Multifractality in high-dimensional graphs induced by correlated radial disorder

David E. Logan^{1,*} and Sthitadhi Roy^{2,†}

¹University of Oxford, Physical and Theoretical Chemistry Laboratory, South Parks Road, Oxford OX13QZ, United Kingdom ²International Centre for Theoretical Sciences, Tata Institute of Fundamental Research, Bengaluru 560089, India

We introduce a class of models containing robust and analytically demonstrable multifractality induced by disorder correlations. Specifically, we investigate the statistics of eigenstates of disordered tight-binding models on two classes of rooted, high-dimensional graphs – trees and hypercubes – with a form of strong disorder correlations we term 'radial disorder'. In this model, site energies on all sites equidistant from a chosen root are identical, while those at different distances are independent random variables (or their analogue for a deterministic but incommensurate potential, a case of which is also considered). Analytical arguments, supplemented by numerical results, are used to establish that this setting hosts robust and unusual multifractal states. The distribution of multifractality, as encoded in the inverse participation ratios (IPRs), is shown to be exceptionally broad. This leads to a qualitative difference in scaling with system size between the mean and typical IPRs, with the latter the appropriate quantity to characterise the multifractality. The existence of this multifractality is shown to be underpinned by an emergent fragmentation of the graphs into effective one-dimensional chains, which themselves exhibit conventional Anderson localisation. The interplay between the exponential localisation of states on these chains, and the exponential growth of the number of sites with distance from the root, is the origin of the observed multifractality.

I. INTRODUCTION

The anatomy of eigenstates of a single quantum particle hopping on disordered, high-dimensional graphs is central to understanding a range of fundamental phenomena in condensed matter and statistical physics. On the one hand, it lies at the heart of the theory of one-body Anderson localisation [1–5], and continues to reveal rich insights into the underlying physics some seven decades after its inception [6–10]. On the other hand, the issue has gained renewed significance with the advent of many-body localisation (MBL), which addresses the fate of Anderson localisation in the presence of interactions and constitutes a novel form of ergodicity breaking in quantum many-body systems [11–17].

The latter reflects the fact that the problem of MBL in archetypal models, such as disordered spin- or fermionic chains, can be mapped exactly onto that of a fictitious single particle on the high-dimensional Fock-space graph of the model [18–36] (see Refs. [37, 38] for reviews and further references); e.g. the Fock-space graph of the disordered tilted-field Ising model with L spins is an L-dimensional hypercube [38]. Although the problems of one- and many-body localisation are inherently different, much cross-pollination of ideas between them has occurred, which has enriched our understanding of MBL [8, 21, 28, 29, 39–43]. Importantly, this has also pinpointed key features of Fock-space graphs, and the structure of eigenstates thereon, which distinguish MBL from conventional Anderson localisation on high-dimensional graphs.

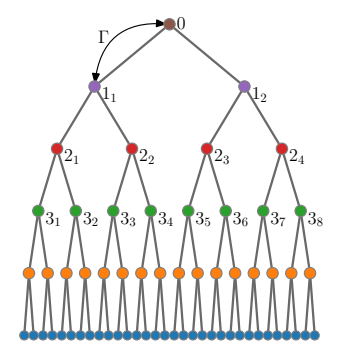
One of the most significant such features is the presence of correlations in the effective disorder on the Fockspace graph [25]. Canonical models of MBL show 'maximally correlated disorder' on the Fock-space graph, which was argued to be a key requirement for the stability of MBL [25]. By this is meant that the disordered site energies on the Fock-space graph, rescaled appropriately to admit a well-defined thermodynamic limit, are completely slaved to each other for sites separated by a finite (Hamming) distance in the thermodynamic limit. The naive expectation would be that correlations leading to increased similarity between nearby site energies would weaken localisation, yet such correlations act to stabilise the MBL phase. The essential message here is that strong correlations in the effective disorder in high-dimensional graphs can render the problem fundamentally different from that of conventional Anderson localisation, and as such provides fruitful ground for further exploration.

From the viewpoint of eigenstate structure, an important understanding is that MBL eigenstates are multifractal on the Fock-space graph [26–28, 30–32, 39, 44, 45]. Wavefunctions of a single particle, fictitious or otherwise, can be broadly classified into three kinds: delocalised, localised, and multifractal. Delocalised states occupy a finite fraction of sites on the graph, whereas localised ones occupy only a finite number of sites, and hence a vanishing fraction in the thermodynamic limit. Multifractal states are essentially intermediate in character, where wavefunctions occupy a number of sites which grows unboundedly but a fraction which vanishes in the thermodynamic limit. In genuine single-particle settings, multifractality is somewhat special as it typically appears at criticality, such as Anderson transitions and inte-

^{*} david.logan@chem.ox.ac.uk

[†] sthitadhi.roy@icts.res.in

 $^{^{\}rm 1}$ Of course, we implicitly assume systems with locality and exclude



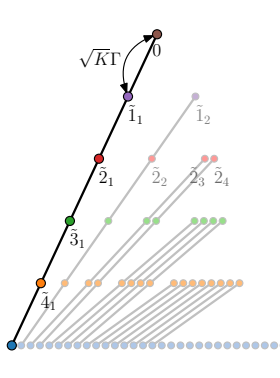


FIG. 1. Left panel: Rooted Cayley tree, illustrated for connectivity K=2. The graph has L+1 rows, with $N_r=K^r$ sites/vertices on row r (and r=0 the root site). Hoppings (bonds/edges) are as indicated, each of strength Γ . With radial disorder, all sites on a given row have the same site energies (indicated by a common colour); while sites on different rows have distinct site energies. Right panel: Corresponding tree under the symmetrised basis transformation specified in Sec. II. Hoppings are again as indicated, all being of strength $\sqrt{K}\Gamma$. The tree has fragmented into a disconnected set of 1d chains. Full discussion in text (see Sec. II A).

ger quantum Hall plateau transitions [5, 50–56]. Quite tellingly though, correlations in the disorder or hopping matrix elements in such settings have turned out to be a source of robust multifractality [42, 57, 58]. On the other hand, in the many-body setting on the Fock space, multifractality is generically robust and often taken as a defining signature of an ergodicity-broken phase [26–28, 30–32, 39, 44, 45].

These considerations illustrate that disorder correlations and the multifractality of wavefunctions – features that arise naturally in many-body systems when represented on the Fock space – are central to a wealth of phenomena in disordered systems. This prompts a natural question: can one construct models of disorder correlations on high-dimensional graphs that not only exhibit robust multifractality but also yield analytical insights into the mechanisms underpinning its emergence? This is the question we address here. We show explicitly that two classes of high-dimensional graphs – trees and hypercubes - can host robust multifractal eigenstates when endowed with a specific class of disorder correlations, which we refer to as radial disorder for reasons that will become clear shortly. We demonstrate that radial disorder induces a hierarchical structure on the graph and leads to its fragmentation into an emergent family of effective one-dimensional chains. The interplay between Anderson localisation on these chains, and the structure that relates them back to the original graph, lies at the heart

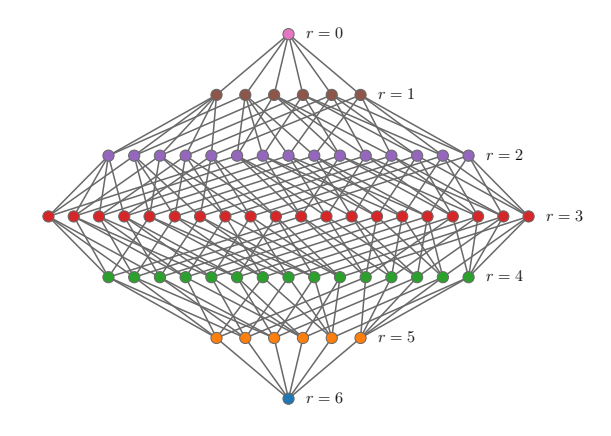


FIG. 2. L-dimensional hypercube graph (illustrated for L=6). The graph has L+1 rows, with $N_r=\binom{L}{r}$ sites/vertices on row r (r=0 is the apex site). Under \hat{H}_{Γ} , hoppings (of strength Γ) connect only sites on adjacent rows. Each site on row r is connected under \hat{H}_{Γ} to L others: to r distinct sites on row (r-1), and to (L-r) sites on row (r+1). With radial disorder, all sites on a given row have the same site energies (indicated by a common colour); while sites on different rows have distinct site energies. For full discussion see Sec. IV.

of the resultant multifractality. These are the central qualitative results of the present work.

A. Tree and hypercube graphs

Before proceeding, it is expedient to summarise the essential properties of the two graphs considered, and lay out some definitions. For the tree graph, we consider a rooted Cayley tree with branching number K, containing L generations and hence L+1 rows denoted $r=0,1,\cdots L$ (with r=0 the root site). The number of sites on row r is $N_r=K^r$, and each such is a Hamming distance of r from the root. The total number of sites/vertices is $N=\sum_{r=0}^L N_r \propto K^L$, exponentially large in L. Since sites on the graph are naturally arranged in rows, we denote the sites on any given row r as $r_1, r_2, \cdots r_{N_r}$. The tree is inherently loopless (cycle-free), and just a single direct hopping path connects any pair of vertices. Fig. 1 (left panel) illustrates a rooted tree with connectivity K=2, and sites on each row labelled as indicated.

The hypercube graph, of dimension L, is also an L-regular graph, with $N=2^L$ sites. Fig. 2 illustrates one with L=6. Note that the dimensionality of the hypercube is also the diameter of the graph (the maximum value of the shortest path length between any pair of sites on the graph) or, equivalently, the number of generations in the graph. Assigning any one site to be the apical site of the hypercube, with r=0, the remaining sites can again be arranged in rows $r\in[1,L]$, with any site on row r lying a Hamming distance r from the apex. Each row now contains $N_r=\binom{L}{r}$ sites, whence a total of

effective random matrix models with long (infinite)-ranged hopping, such as power-law banded matrices, the Rosenzweig-Porter model or random Erdös-Rényi graphs, which do host robust multifractality $[5,\ 46-49]$.

 $N=2^L$ sites. Any given site on row r is connected by r edges to r distinct sites in row r-1, and by L-r edges to L-r distinct sites in row r+1. In contrast to the tree, any site on row r is connected to the apex site by r! distinct paths. As with the tree, we denote the set of sites on any given row r as $\{r_n\}$ with $n=1,2,\cdots N_r$.

Given the above topology of the tree and hypercube graphs, we will consider tight-binding models (TBM) defined on them. They are described the Hamiltonian

$$\hat{H} = \sum_{i} \mathcal{E}_{i} |i\rangle\langle i| + \Gamma \sum_{(i,j)} |i\rangle\langle j| \equiv \hat{H}_{0} + \hat{H}_{\Gamma}, \quad (1)$$

where nearest neighbour pairs of sites (denoted by (i, j)) have a constant hopping matrix element Γ , and the site energies $\{\mathcal{E}_i\}$ are disordered. Note that the topology of the graphs guarantees that for a pair of sites to be nearest neighbours, they must reside on consecutive rows.

Two remarks are in order here. In the limit where all the N site-energies \mathcal{E}_i are i.i.d. random variables, the model on the tree reduces to the extensively studied Anderson localisation problem on a tree [2, 59-68] which hosts a localisation transition at a finite critical disorder strength and, more importantly in the present context, a fully delocalised phase at sufficiently weak but nonvanishing disorder. In the same uncorrelated limit, the problem on the hypercube [25] is essentially the quantum random energy model [69–71], which is ergodic except at the edges of the many-body spectrum for all disorder strengths. By contrast, with radially correlated disorder, we find the emergence of multifractality for any non-zero disorder strength for both the tree and hypercube graphs; and throughout the range of parameters in the incommensurate case which corresponds to the localised phase of the 1d Aubry-André model. This attests to the emergent multifractality being induced by the radial disorder.

B. Radial disorder

Let us now define concretely the notion of radial disorder. The notation for labelling the set of sites on row r as $\{r_n\}$ implies that the diagonal part of the Hamiltonian in Eq. 1, for both the tree and the hypercube, can be expressed as

$$\hat{H}_{0} = \sum_{r=0}^{L} \hat{H}_{0,r} = \sum_{r=0}^{L} \sum_{n=1}^{N_{r}} \mathcal{E}_{r_{n}} |r_{n}\rangle\langle r_{n}|, \qquad (2)$$

with $N_r = K^r$ for the tree and $N_r = {L \choose r}$ for the hypercube. Radial disorder refers to a particular form of correlation in the site energies $\{\mathcal{E}_{r_n}\}$, whereby the site energies on all sites of a given row are the same. Formally,

$$\mathcal{E}_{r_n} = \mathcal{E}_r \ \forall n \in [1, N_r], \tag{3}$$

where the set $\{\mathcal{E}_r\}$ are treated as independent, quenched random variables. In addition we will also consider (Sec.

III) the case where, instead of quenched disorder, the $\{\mathcal{E}_r\}$ are given by a deterministic but incommensurate (in r) potential, as per the Aubry-André model [72].

C. Measures of multifractality

It is prudent at this stage to make a general remark about the multifractality found in this work. Multifractality of wavefunctions is most commonly studied using the scaling of the inverse participation ratio (IPR) with the system size, N. The q^{th} -IPR for a state $|\psi\rangle = \sum_{i=1}^{N} \psi_i |i\rangle$ is defined as

$$\mathcal{L}_q = \sum_{i=1}^N |\psi_i|^{2q} \,. \tag{4}$$

In the context of disordered systems, it is quite common to consider the average IPR, $\mathcal{L}_q^{\text{mean}} = \langle \mathcal{L}_q \rangle$ where $\langle \cdots \rangle$ denotes an average over disorder realisations. The multifractal exponent is then defined by the scaling of $\mathcal{L}_q^{\text{mean}} \sim N^{-\tau_q^{\text{mean}}}$ with N. An implicit assumption here, one that is often justified, is that the IPRs have a well-behaved distribution.

However, as will be shown explicitly, this is not the case for the models considered in this work: the IPR distributions are found to be very broad (with a mean $\mathcal{L}_q^{\text{mean}}$ that is not in fact remotely representative of the distribution). As a result, it is the typical IPRs, defined via the geometric mean

$$\mathcal{L}_q^{\text{typ}} = \exp\left[\langle \ln \mathcal{L}_q \rangle\right] , \qquad (5)$$

which are the relevant quantities to study; with multifractal exponents defined via the scaling $\mathcal{L}_q^{\mathrm{typ}} \sim N^{-\tau_q}$.

Organisation of the paper

The remainder of the paper is organised as follows. In Sec. II we present in detail the case of tree graphs. The fragmentation of the graph, understood most easily for the disorder-free case, is discussed in Sec. II A. and the persistence of fragmentation in the presence of radial disorder is shown in Sec. IIB; the resultant connection to a Krylov basis is also pointed out. Analytical results for the multifractal statistics, based on the interplay between localisation of states on the effective 1d chain and the hierarchical nature of the original graph. are obtained in Sec. IIC; while numerical calculations from exact diagonalisation (ED), which corroborate these results, are given in Sec. IID. The case of the incommensurate, Aubry-André-like potential for \mathcal{E}_r on the tree graph comprises Sec. III. Analytical considerations in this context are discussed in Sec. III A, followed by ED results in Sec. III B.

Sec. IV is dedicated to the hypercube graph. Despite its obvious difference in topology compared to the Cayley

tree, we show explicitly that the graph again fragments, first for the disorder-free case and then with radial disorder. Using this, analytical results for the multifractal statistics are presented in Sec. IV A, whereas Sec. IV B contains numerical corroborations from ED. We conclude with a summary and some remarks in Sec. V.

II. CAYLEY TREES

We turn now to Cayley trees. In considering such, of natural interest are properties which involve the root site, such as the nature of the eigenstates in which it participates, or the return probability $P_0(t)$. Before considering the radial disorder, let us look first at the case $\hat{H}_0 \equiv 0$ where the site energies are all the same, so that $\hat{H} \equiv \hat{H}_{\Gamma}$ involves solely the hopping parts of the TBM. This may seem (and is) simple, but it is also revealing.

A. Disorder-free tree, $\hat{H} \equiv \hat{H}_{\Gamma}$

All relevant points we want to make can be illustrated by considering a rooted tree of connectivity K=2, shown in Fig. 1 (left). From the basis states in each row/generation, alternative orthonormal sets can be constructed, starting from row 1. For this row, define

$$|\tilde{1}_{1}\rangle = \frac{1}{\sqrt{2}}|1_{1} + 1_{2}\rangle, \quad |\tilde{1}_{2}\rangle = \frac{1}{\sqrt{2}}|1_{1} - 1_{2}\rangle \quad (6)$$

(with notation $|1_1+1_2\rangle\equiv |1_1\rangle+|1_2\rangle$ etc). The basic idea is to start from the definition $|\tilde{1}_1\rangle$ of the totally symmetric combination of orbitals on row 1, because it is solely this combination to which the root orbital couples under \hat{H}_{Γ} ; with $|\tilde{1}_2\rangle$ then taken to be orthogonal to $|\tilde{1}_1\rangle$. From Eq. 6 the matrix element of \hat{H}_{Γ} coupling the $|0\rangle$ and $|\tilde{1}_1\rangle$ orbitals is clearly $\langle 0|\hat{H}|\tilde{1}_1\rangle=\frac{1}{\sqrt{2}}\langle 0|\hat{H}_{\Gamma}|1_1+1_2\rangle=\sqrt{2}\Gamma$. The generalisation of the totally symmetric $|\tilde{1}_1\rangle$ to arbitrary connectivity is

$$|\tilde{1}_1\rangle = \frac{1}{\sqrt{K}} \sum_{n=1}^{K} |1_n\rangle \implies \langle 0|\hat{H}|\tilde{1}_1\rangle = \sqrt{K}\Gamma \quad (7)$$

with corresponding matrix element $\sqrt{K}\Gamma$. For row r=2 (Fig. 1) one can construct an orthonormal set of $K^2=4$ orbitals $|\tilde{2}_n\rangle$,

$$\begin{split} |\tilde{2}_{1}\rangle &= \frac{1}{2}|2_{1} + 2_{2} + 2_{3} + 2_{4}\rangle \\ |\tilde{2}_{2}\rangle &= \frac{1}{2}|2_{1} + 2_{2} - 2_{3} - 2_{4}\rangle \\ |\tilde{2}_{3}\rangle &= \frac{1}{2}|2_{1} - 2_{2} + 2_{3} - 2_{4}\rangle \\ |\tilde{2}_{4}\rangle &= \frac{1}{2}|2_{1} - 2_{2} - 2_{3} + 2_{4}\rangle. \end{split} \tag{8}$$

Once again, $|\tilde{2}_1\rangle$ is the totally symmetric combination of row-2 orbitals; and it is this combination alone which couples to the $|\tilde{1}_1\rangle$ orbital under $\hat{H}=\hat{H}_{\Gamma}$, with matrix

element $\langle \tilde{1}_1 | \hat{H}_{\Gamma} | \tilde{2}_1 \rangle = \sqrt{2}\Gamma$ again. Similarly, it is solely the $|\tilde{2}_2\rangle$ orbital to which $|\tilde{1}_2\rangle$ (Eq. 6) couples under \hat{H}_{Γ} , again with $\langle \tilde{1}_2 | \hat{H}_{\Gamma} | \tilde{2}_2 \rangle = \sqrt{2}\Gamma$. By contrast, neither $|\tilde{2}_3\rangle$ nor $|\tilde{2}_4\rangle$ couple under \hat{H}_{Γ} to the row-1 orbitals. The process continues in an obvious manner. Row r=3 (Fig. 1) has an orthonormal set of $K^3=8$ orbitals, four of which are

$$\begin{split} |\tilde{3}_{1}\rangle &= \frac{1}{2\sqrt{2}}|3_{1} + 3_{2} + 3_{3} + 3_{4} + 3_{5} + 3_{6} + 3_{7} + 3_{8}\rangle \\ |\tilde{3}_{2}\rangle &= \frac{1}{2\sqrt{2}}|3_{1} + 3_{2} + 3_{3} + 3_{4} - 3_{5} - 3_{6} - 3_{7} - 3_{8}\rangle \\ |\tilde{3}_{3}\rangle &= \frac{1}{2\sqrt{2}}|3_{1} + 3_{2} - 3_{3} - 3_{4} + 3_{5} + 3_{6} - 3_{7} - 3_{8}\rangle \\ |\tilde{3}_{4}\rangle &= \frac{1}{2\sqrt{2}}|3_{1} + 3_{2} - 3_{3} - 3_{4} - 3_{5} - 3_{6} + 3_{7} + 3_{8}\rangle. \end{split} \tag{9}$$

The totally symmetric combination $|\tilde{3}_1\rangle$ couples under \hat{H}_{Γ} solely to the totally symmetric $|\tilde{2}_1\rangle$ orbital of row 2. Similarly, $|\tilde{3}_n\rangle$ for given n=2,3,4 is the only combination which couples to $|\tilde{2}_n\rangle$, again with $\langle \tilde{2}_n|\hat{H}_{\Gamma}|\tilde{3}_n\rangle = \sqrt{2}\Gamma$. By contrast, the $|\tilde{3}_n\rangle$'s with n=5-8 (not given here) do not couple under \hat{H}_{Γ} to any of the row-2 orbitals; and if this was the terminal generation (L) of the tree, they would be completely unconnected under \hat{H}_{Γ} .

Fig. 1 (right panel) shows the resultant connections under \hat{H}_{Γ} between the transformed basis states. And this generalises in an obvious way to arbitrary K, all non-zero matrix elements under \hat{H}_{Γ} being $\sqrt{K}\Gamma$ (as e.g. in Eq. 7).

With this transformation, the problem has clearly fragmented into a disconnected set of 1d chains, whence knowledge of the pure 1d case (K=1) suffices to understand the behaviour of a tree with arbitrary K. In particular, the sector containing the 0-orbital is a 1d chain in terms of the set $\{|\tilde{r}_1\rangle\}$ of totally symmetric basis orbitals associated with any row $r \in [0, L]$ of the tree,

$$|\tilde{r}_1\rangle = \frac{1}{\sqrt{N_r}} \sum_{n=1}^{N_r} |r_n\rangle$$
 (10)

(with $N_r = K^r$, and notation $|\tilde{0}_1\rangle \equiv |0_1\rangle \equiv |0\rangle$ for r = 0); but with a nearest neighbour hopping matrix element which is $\sqrt{K}\Gamma$ rather than Γ itself. The associated separable part of the Hamiltonian, denoted $\hat{\mathcal{H}}_{\Gamma}$, is

$$\hat{\mathcal{H}}_{\Gamma} = \sqrt{K}\Gamma \sum_{r=1}^{L} \left(|\widetilde{(r-1)}_{1}\rangle \langle \tilde{r}_{1}| + \text{h.c.} \right).$$
 (11)

So e.g. the return probability $P_0(t)$ is consequently of form $P_0(t) = F(\sqrt{K}\Gamma t)$, with $F(\Gamma t)$ the return probability for a 1d chain with K=1. From this, on calculating the underlying root-site propagator $G_{00}(t)$ (such that $P_0(t) = |G_{00}(t)|^2$), one obtains straightforwardly the exact return probability for $L \to \infty$,

$$P_0(\tilde{t}) = \left[\frac{1}{\tilde{t}}J_1(2\tilde{t})\right]^2 \stackrel{\tilde{t} \gg 1}{\sim} \frac{1}{\pi \tilde{t}^3} \cos^2\left[2\tilde{t} - \frac{3\pi}{4}\right]$$
 (12)

with $\tilde{t} = \sqrt{K}\Gamma t$ (and $J_1(x)$ a first-kind Bessel function). As expected physically, $P_0(\tilde{t})$ vanishes as $\tilde{t} \to \infty$; and does so with a power-law decay $\propto \tilde{t}^{-3}$ superimposed on an oscillatory background. Generalising this by the same means to the probability $P_r(\tilde{t})$ that the system will be found on row r of the chain (with $P_r(\tilde{t}=0) = \delta_{r,0}$), gives

$$P_r(\tilde{t}) = \left[\frac{(1+r)}{\tilde{t}}J_{1+r}(2\tilde{t})\right]^2 : \tilde{t} = \sqrt{K}\Gamma t, \quad (13)$$

recovering Eq. 12 for r=0. Note also that in terms of the original tree basis $\{|r_n\rangle\}$, and due to the above fragmentation, $P_r(\tilde{t}) \equiv \sum_{n=1}^{K^r} P_{r_n}(\tilde{t})$ is equivalently the total probability that the system will be found on any of the N_r sites $\{r_n\}$ on row r of the tree.

The system's mean position $\bar{r}(\tilde{t})$ on the chain/tree, following initiation on the root site at $\tilde{t} = 0$, is simply

$$\overline{r}(\tilde{t}) = \sum_{r=0}^{\infty} r P_r(\tilde{t}) \stackrel{\tilde{t} \ge 1}{\sim} v\tilde{t}.$$
 (14)

Using Eq. 13, this gives $\overline{r}(\tilde{t}) \sim \tilde{t}^2$ for short times $\tilde{t} \lesssim 1$; but for $\tilde{t} \gtrsim 1$ it rapidly crosses over to the ballistic transport $\overline{r}(\tilde{t}) = v\tilde{t}$, with dimensionless velocity v = 1.70...

1. Connection to Krylov basis

The findings above are closely connected to the notion of a Krylov basis, and the associated Krylov Hamiltonian [73–76]. Quite generally, to define a Krylov space requires an initial state $|k_0\rangle$ and an operator, here the Hamiltonian \hat{H} . The space is constructed by repeated application of \hat{H} on $|k_0\rangle$, to generate $|\tilde{k}_r\rangle = \hat{H}^r|k_0\rangle$. Applying the Gram-Schmidt procedure to mutually orthonormalise all $|\tilde{k}_r\rangle$ then generates an orthonormal basis $|k_r\rangle$, the Krylov basis $\mathcal{K}(\hat{H},|k_0\rangle) = \text{span}\{|k_r\rangle: r = 0,1,2,\cdots\}$. Starting from $|k_0\rangle$, the $\{|k_r\rangle\}$ are obtained from the linear recurrence

$$b_{r+1}|k_{r+1}\rangle \ = \ \left(\hat{H}-a_r\right)|k_r\rangle-b_r|k_{r-1}\rangle \eqno(15)$$

with $b_0 = 0$. The Hamiltonian in the Krylov basis – the Krylov Hamiltonian – is by construction tridiagonal (its non-zero elements being the Lanczos coefficients), i.e. it has the form of a 1d chain, with off-diagonal matrix elements $b_r = \langle k_{r-1}|\hat{H}|k_r\rangle$ and diagonals $a_r = \langle k_r|\hat{H}|k_r\rangle$.

In the present context, taking $|k_0\rangle = |0\rangle$ as the root site of the Cayley tree, it is readily shown using Eq. 15 with $\hat{H} \equiv \hat{H}_{\Gamma}$ that the resultant Krylov basis is precisely the set $\{|\tilde{r}_1\rangle\}$ of totally symmetric orbitals (Eq. 10), and that the Krylov Hamiltonian is what we have denoted by $\hat{\mathcal{H}}_{\Gamma}$ in Eq. 11 (with $b_r = \sqrt{K}\Gamma$ and $a_r = 0$). Further, $\bar{r}(\hat{t})$ given in Eq. 14 is precisely the so-called Krylov spread complexity, quantifying spatiotemporal spread of a wavefunction following initiation on $|0\rangle$; and study of which has seen a recent surge of popularity in a wide range of physical contexts (see e.g. the review [76]).

B. Radially disordered tree

So far, the 'pure hopping' case $\hat{H} \equiv \hat{H}_{\Gamma}$ has been considered. Now we include the radial disorder. Here, as mentioned in Sec. IA, the site energies in any given row r are (by definition) so strongly correlated that they are completely slaved to each other, viz $\mathcal{E}_{r_n} = \mathcal{E}_r$ independently of n. Eq. 2 for \hat{H}_0 then reads $\hat{H}_0 = \sum_{r=0}^L \mathcal{E}_r \hat{1}_r$ with $\hat{1}_r = \sum_{n=1}^{N_r} |r_n\rangle \langle r_n|$ the projector for row r. Since, for any r and m, the states $|\tilde{r}_m\rangle$ of Sec. II A are composed solely of tree orbitals $\{|r_n\rangle\}$ from row r, they satisfy $|\tilde{r}_m\rangle = \hat{1}_r|\tilde{r}_m\rangle$; and thus $\hat{H}_0|\tilde{r}_m\rangle = \mathcal{E}_r|\tilde{r}_m\rangle$ and $\langle \tilde{r}'_{m'}|\hat{H}_0|\tilde{r}_m\rangle = \mathcal{E}_r\delta_{r'r}\delta_{m'm}$.

Hence, exactly the same fragmentation into 1d chains as arises under \hat{H}_{Γ} alone persists in the presence of radial disorder. In particular, the separable part of the Hamiltonian which contains the root site, denoted by $\hat{\mathcal{H}} = \hat{\mathcal{H}}_0 + \hat{\mathcal{H}}_{\Gamma}$, is

$$\hat{\mathcal{H}} = \sum_{r=0}^{L} \mathcal{E}_r |\tilde{r}_1\rangle \langle \tilde{r}_1| + \sqrt{K}\Gamma \sum_{r=1}^{L} \left(|\widetilde{(r-1)}_1\rangle \langle \tilde{r}_1| + \text{h.c.} \right). \tag{16}$$

And once again, with $|k_0\rangle = |0\rangle$, it follows from Eq. 15 using the full $\hat{H} = \hat{H}_0 + \hat{H}_{\Gamma}$ that the Krylov basis is the set $\{|\tilde{r}_1\rangle\}$ of totally symmetric orbitals (Eq. 10), and that Eq. 16 is the Krylov Hamiltonian (now with $a_r = \mathcal{E}_r$ and $b_r = \sqrt{K}\Gamma$).

We focus on $\hat{\mathcal{H}}$ – a 1d tight-binding chain in the \tilde{r}_1 -basis, with constant nearest neighbour hopping $\sqrt{K}\Gamma$, and a total of L+1 site energies \mathcal{E}_r . Taking the $\{\mathcal{E}_r\}$ as i.i.d. random variables with distribution $P_{\mathcal{E}}(\mathcal{E})$, all states are in consequence exponentially localised on the chain for any disorder strength W>0 (and any finite K). As elaborated below, rather than enhancing delocalisation – as one might intuitively have guessed – introducing strong correlations in the site-energies of the Cayley tree in this way in fact does just the opposite.

In the following, our interest will centre on the localisation characteristics of the eigenstates $|\psi_E\rangle$ of $\hat{\mathcal{H}}$ on the tree – i.e. in the tree basis $\{|r_n\rangle\}$ – as embodied in the corresponding inverse participation ratios (IPRs) \mathcal{L}_q specified below. In the \tilde{r}_1 -basis of totally symmetric tree orbitals (Eq. 10), localisation properties on the associated 1d chain are of course quite simple, since

$$|\psi_E\rangle = \sum_{r=0}^{L} A_{E,r} |\tilde{r}_1\rangle \tag{17}$$

where $|A_{E,r}|^2 \propto e^{-|r-r_E|/\xi}$ decays exponentially about its localisation centre $r=r_E$ with a finite localisation length, ξ . As a result, IPRs in the \tilde{r}_1 -basis, $L_q=\sum_{r=0}^L |A_{E,r}|^{2q}$ (on which we touch briefly below), are all finite and L-independent.

But equally, one can decompose $|\psi_E\rangle$ in the tree basis,

$$|\psi_E\rangle = \sum_{r=0}^L \sum_{n=1}^{N_r} A_{E,r_n} |r_n\rangle, \tag{18}$$

with associated IPRs

$$\mathcal{L}_q(r_E) = \sum_{r=0}^{L} \sum_{r=1}^{N_r} |A_{E,r_n}|^{2q}.$$
 (19)

Using Eq. 10 in Eq. 17 then relates A_{E,r_n} to $A_{E,r}$, viz.

$$A_{E,r_n} = A_{E,r} / \sqrt{N_r} \tag{20}$$

(for all $n \in [1, N_r]$), and hence

$$\mathcal{L}_q(r_E) = \sum_{r=0}^{L} \frac{|A_{E,r}|^{2q}}{N_r^{q-1}}.$$
 (21)

From a numerical viewpoint, direct calculations on trees are limited (by the tree dimension $N \sim K^L$) to rather modest values of $L \lesssim 20$ or so. Eq. 21 by contrast allows much larger L's to be reached, by first obtaining the $\{A_{E,r}\}$ for a 1d chain of length L, and then performing the sums to give \mathcal{L}_q . We employ this in later sections.

More importantly, Eq. 21 enables some insight to be obtained analytically, as now considered.

C. Analytical considerations

As mentioned above, the square amplitude

$$|A_{E,r}|^2 = \frac{1}{\mathcal{N}} e^{-|r-r_E|/\xi}$$
 (22)

decays exponentially about its localisation centre r_E , with localisation length ξ . The normalisation constant \mathcal{N} then follows from $\sum_{r=0}^{L} |A_{E,r}|^2 = 1$,

$$\mathcal{N} = \frac{e^{1/\xi} + 1 - e^{-r_E/\xi} - e^{-(L-r_E)/\xi}}{e^{1/\xi} - 1}.$$
 (23)

In the 1d chain of length $L\gg 1$, localised states of given energy can of course coexist for a given disorder realisation, being centred on different parts of the chain and thus having different localisation centres r_E . Over an ensemble of disorder realisations, it is the distribution of r_E 's that is sampled when considering all states of some energy E. We assume that each such r_E is equally probable, i.e. its distribution is $P_{r_E}(r_E) = L^{-1}\Theta(r_E)\Theta(L-r_E)$ (with $\Theta(x)$ the unit step function). Given this, the probability that r_E lies within a distance $\mathcal{O}(1)$ of the chain ends (r=0,L) is $\propto 1/L$ and thus neglectable as $L\to\infty$, while the corresponding probability that r_E is of order L is unity. In that case, the above expression for $\mathcal N$ reduces in practice to

$$\mathcal{N} = \frac{e^{1/\xi} + 1}{e^{1/\xi} - 1} = \coth\left(\frac{1}{2\xi}\right),\tag{24}$$

which we generally use in the following. With the same reasoning, the IPRs in the \tilde{r}_1 -basis can be obtained, and are given by

$$L_q = \sum_{r=0}^{L} |A_{E,r}|^{2q} = \left[\tanh\left(\frac{1}{2\xi}\right) \right]^q \coth\left(\frac{q}{2\xi}\right). \quad (25)$$

As noted earlier, the L_q are finite and L-independent (because eigenstates in the \tilde{r}_1 -basis are localised on the 1d chain on the lengthscale $\xi \sim \mathcal{O}(1)$).

Now consider the main quantities of interest, the IPRs in the original tree basis, Eq. 21. This gives $\mathcal{L}_q(r_E)$ for an eigenstate with localisation centre r_E . Over an ensemble of disorder realisations, and hence over the distribution of r_E , \mathcal{L}_q will be characterised by its distribution $P_{\mathcal{L}_q}(\mathcal{L}_q)$, the form of which we obtain below. Two particular measures of that distribution will be considered, namely the typical value $\mathcal{L}_q^{\text{typ}}$ (geometric mean) and the arithmetic mean $\mathcal{L}_q^{\text{mean}}$; calculated respectively from

$$\ln \mathcal{L}_{q}^{\text{typ}} = \frac{1}{L+1} \sum_{r_{E}=0}^{L} \ln \mathcal{L}_{q}(r_{E}) \equiv \left\langle \ln \mathcal{L}_{q}(r_{E}) \right\rangle_{r_{E}}$$

$$\mathcal{L}_{q}^{\text{mean}} = \frac{1}{L+1} \sum_{r_{D}=0}^{L} \mathcal{L}_{q}(r_{E}) \equiv \left\langle \mathcal{L}_{q}(r_{E}) \right\rangle_{r_{E}}$$
(26)

(with the right hand sides an obvious shorthand).

With $|A_{E,r}|^2$ from Eq. 22, Eq. 21 for $\mathcal{L}_q(r_E)$ can be evaluated in full (recall that $N_r = K^r$). This yields

$$\mathcal{N}^{q} \mathcal{L}_{q}(r_{E}) = \frac{K^{(q-1)} e^{-\frac{qr_{E}}{\xi}} - e^{\frac{q}{\xi}} e^{-r_{E}(q-1)\ln K}}{\left[K^{(q-1)} - e^{\frac{q}{\xi}}\right]} + \frac{e^{-(q-1)r_{E}\ln K}}{\left[K^{(q-1)} e^{\frac{q}{\xi}} - 1\right]} \left[1 - e^{-(L-r_{E})[(q-1)\ln K + \frac{q}{\xi}]}\right].$$
(27)

For use below, let us first look at this in the two cases of $\xi \ll 1$ and $\xi \gg 1$, corresponding physically to strong and weak disorder strengths respectively; and considering that r_E is $\propto L$ with probability unity (as discussed above). For the present, we also have in mind q>1 (q=2) being the most commonly encountered IPR). Consider first $\xi \ll 1$ (more precisely $\xi \ll q/[(q-1)\ln K])$. Here, Eq. 27 reduces asymptotically to

$$\mathcal{L}_q(r_E) \stackrel{\xi \lesssim 1}{\sim} e^{-r_E(q-1)\ln K} \left[1 + \mathcal{O}\left(e^{-q/\xi}\right) \right]$$
 (28)

(using also $\mathcal{N} \sim 1$ for $\xi \ll 1$, see Eq. 24). For $\xi \gg 1$ by contrast, Eq. 27 gives to leading order that

$$\mathcal{L}_q(r_E) \stackrel{\xi \gg 1}{\sim} \frac{1}{(2\xi)^q} \frac{1}{[1 - K^{-(q-1)}]} \exp\left(-\frac{qr_E}{\xi}\right)$$
 (29)

(with $\mathcal{N} = 2\xi + \mathcal{O}(1)$ in this case).

Fig. 3 shows the mean and typical IPRs for q=2 (with K=2), computed using Eq. 26 and the full Eq. 27 for $\mathcal{L}_q(r_E)$, over the wide range of ξ 's indicated. The mean, $\mathcal{L}_2^{\text{mean}}$, is plotted against the total number of tree generations, L; while the typical, $\mathcal{L}_2^{\text{typ}}$, is shown vs the total number of sites on the tree N, given by

$$N = \sum_{r=0}^{L} K^{r} \overset{L \gg 1}{\sim} \frac{K}{K - 1} K^{L}. \tag{30}$$

Three features in Fig. 3 stand out:

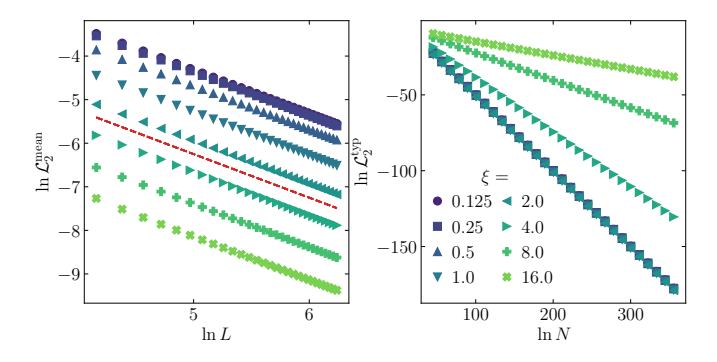


FIG. 3. Mean $\mathcal{L}_2^{\mathrm{mean}}$ (left) and typical $\mathcal{L}_2^{\mathrm{typ}}$ (right) IPR for q=2 (with K=2), computed from the full analytical expressions in Eqs. 27,26 over the range of ξ indicated. $\mathcal{L}_2^{\mathrm{mean}}$ is plotted vs the total number of tree generations, L, while $\mathcal{L}_2^{\mathrm{typ}}$ is plotted against the total number of sites on the tree, $N \propto K^L$. Red dashed line in the $\ln \mathcal{L}_2^{\mathrm{mean}}$ plot indicates a slope of -1.

- 1. $\mathcal{L}_2^{\text{mean}}$ decays as a power-law in the number of generations L, specifically $\mathcal{L}_2^{\text{mean}} \propto L^{-1}$. In contrast, $\mathcal{L}_2^{\text{typ}}$ decays as a power-law in the total number of tree sites N.
- 2. $\mathcal{L}_2^{\text{typ}}$ is many orders of magnitude smaller than $\mathcal{L}_2^{\text{mean}}$, suggesting a very broad distribution of IPRs.
- 3. With increasing localisation length ξ , the state spreads out more on the chain, so one expects the IPR to decrease. $\mathcal{L}_2^{\text{mean}}$ indeed shows this trend. By contrast, $\mathcal{L}_2^{\text{typ}}$ quite remarkably shows the opposite trend, increasing with increasing ξ .

To understand these features, let us analyse the behaviour in the two limits of large and small ξ . For $\xi \ll 1$, using the leading behaviour $\mathcal{L}_q(r_E) \sim K^{-(q-1)r_E}$ of Eq. 28 in Eq. 26 gives

$$\mathcal{L}_q^{\mathrm{mean}} \overset{L \gg 1}{\sim} \frac{1}{[1 - K^{-(q-1)}]} \frac{1}{L} \propto \frac{1}{L} \quad : \xi \ll 1 \quad (31\mathrm{a})$$

$$\mathcal{L}_{q}^{\text{typ}} \overset{L \gg 1}{\sim} \exp \left[-\frac{1}{2} (q-1) L \ln K \right] \sim N^{-\frac{1}{2}(q-1)}; (31b)$$

while for $\xi \gg 1$, Eq. 29 used in Eq. 26 gives

$$\mathcal{L}_{q}^{\text{mean } L \gg 1} \frac{1}{(2\xi)^{q}} \frac{1}{[1 - K^{-(q-1)}]} \frac{1}{[1 - e^{-q/\xi}]} \frac{1}{L} \propto \frac{1}{L} \quad (32a)$$

$$\mathcal{L}_{q}^{\text{typ } L \gg 1} \frac{1}{(2\xi)^{q}} \frac{1}{[1 - K^{-(q-1)}]} \frac{1}{L} \exp\left[-\frac{q}{2\xi}L\right]$$

$$\sim N^{-q/(2\xi \ln K)} \quad : \quad \xi \gg 1. \quad (32b)$$

Whether ξ is large or small, Eqs. 31a,32a show that $\mathcal{L}_q^{\text{mean}} \propto 1/L$, as indeed seen in Fig. 3 for any ξ . As also seen in Fig. 3, Eqs. 31b,32b likewise show that $\mathcal{L}_q^{\text{typ}}$ scales as a power-law in the total number of tree sites N,

$$\mathcal{L}_q^{\text{typ}} = N^{-\tau_q}. \tag{33}$$

This of course is multifractal behaviour of the eigenstates, with multifractal exponent τ_q ; such behaviour being manifest in the typical value of \mathcal{L}_q , but not in the mean $\mathcal{L}_q^{\text{mean}}$. The exponents τ_q can be read off from Eqs. 31b,32b,

$$\tau_q(\xi) = \begin{cases} \frac{1}{2}(q-1) & : \xi \ll 1\\ \frac{q}{2\xi \ln K} & : \xi \gg 1. \end{cases}$$
 (34)

This behaviour is indeed seen clearly in Fig. 4 (right panel), where the ξ -dependence of τ_q is shown for three different q's. Eq. 34 is in fact more general than its asymptotic derivation here. Within the present framework, the exact $\tau_q(\xi)$ can be obtained and are given in Sec. II C 1. In particular, for any $q \geq 1$, the form Eq. 34 is more generally correct: $\tau_q = \frac{1}{2}(q-1)$ holds for all $\xi \ln K \leq q/(q-1)$, and likewise $\tau_q = q/(2\xi \ln K)$ for all $\xi \ln K > q/(q-1)$ (Eq. 41).

As noted in point 2 above, Fig. 3 shows $\mathcal{L}_2^{\text{typ}}$ to be many orders of magnitude smaller than $\mathcal{L}_2^{\text{mean}}$, suggesting a very broad distribution of IPRs. To understand this, note from Eqs. 28,29 that, whether $\xi \ll 1$ or $\xi \gg 1$, the IPR as a function of r_E is of form

$$\mathcal{L}_{q}(r_{E}) = c_{1}e^{-c_{2}r_{E}} \tag{35}$$

where c_1, c_2 (each positive for $q \geq 1$ and with $c_1 \leq 1$) depend on q, K and ξ . Given that each $r_E \in [0, L]$ is equally probable over an ensemble of disorder realisations, the probability distribution of IPRs, $P_{\mathcal{L}_q}(\mathcal{L}_q) = \int dr \ P_{r_E}(r) \delta(\mathcal{L}_q - c_1 e^{-c_2 r})$, follows as

$$P_{\mathcal{L}_q}(\mathcal{L}_q) = \frac{1}{\mathcal{L}_q} (c_2 L)^{-1} \Theta \left(\mathcal{L}_q - c_1 e^{-c_2 L} \right) \Theta \left(c_1 - \mathcal{L}_q \right). \tag{36}$$

The important point here is the universal $1/\mathcal{L}_q$ decay in the distribution, 2 reflecting the broad distribution of localisation centres r_E . As a result of this heavy-tailed behaviour, the average value $\mathcal{L}_q^{\text{mean}} \equiv \int d\mathcal{L}_q \ \mathcal{L}_q P_{\mathcal{L}_q}(\mathcal{L}_q) = (c_2 L)^{-1} [c_1 - c_1 e^{-c_2 L}] \sim (c_1/c_2) L^{-1}$ is controlled by the $\mathcal{O}(1)$ values of \mathcal{L}_q (and is thus overall $\propto 1/L$). But $\mathcal{O}(1)$ values of \mathcal{L}_q have a vanishing probability of occurrence as $L \to \infty$, so the mean is thus dominated by occurrences which are statistically irrelevant. Typical occurrences by contrast are those for which \mathcal{L}_q is exponentially small in L. One sees this clearly by looking at the fraction of the distribution which lies between x and its upper limit of c_1 , namely

$$F_{\mathcal{L}_q}(x) = \int_x^{c_1} d\mathcal{L}_q \ P_{\mathcal{L}_q}(\mathcal{L}_q) = \frac{1}{c_2 L} \ln \left[\frac{c_1}{x} \right]. \quad (37)$$

If x is $\mathcal{O}(1)$, then $F_{\mathcal{L}_q}(x) \propto 1/L$ thus vanishes as $L \to \infty$. By contrast, $F_{\mathcal{L}_q}(x)$ is finite as $L \to \infty$ only if $x \propto 1/L$

 $^{^2}$ $P_{\mathcal{L}_q}(\mathcal{L}_q)$ has of course bounded support: \mathcal{L}_q is positive by definition, and for $q \geq 1$ no \mathcal{L}_q can exceed 1, so the distribution is bounded from above by $c_1 \sim \mathcal{O}(1)$, and from below by a value exponentially small in L.

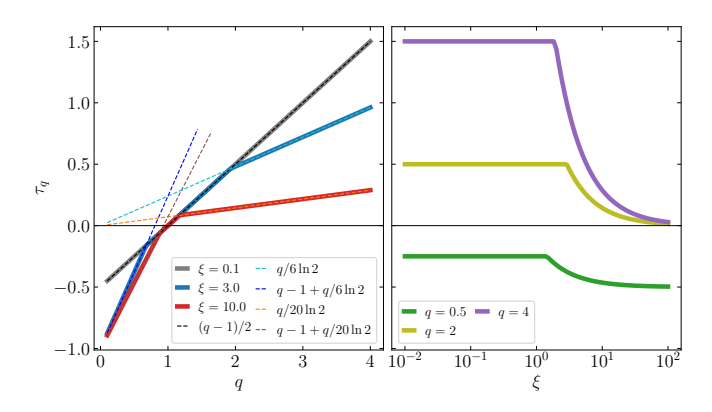


FIG. 4. Left panel: multifractal exponent τ_q as a function of q, shown for $\xi=0.1,3$ and 10 (with K=2). Solid lines show results computed numerically via Eqs. 33,26 using the full sum expression in Eq. 27, while dashed lines show the exact results given in Sec. II C 1 (Eq. 38 for $\xi=3,10$, and Eq. 40 for $\xi=0.1$); the two are indistinguishable. Right panel: τ_q vs ξ , shown for q=4,2 and 0.5,and given exactly by Eq. 41 for q=2,4 and Eq. 42 for q=1/2.

 $e^{-\alpha L}$ is exponentially small in L. In other words, the bulk of the distribution $P_{\mathcal{L}_q}(\mathcal{L}_q)$ occurs for exponentially small values of \mathcal{L}_q . It is of course for this reason that the geometric mean $\mathcal{L}_q^{\text{typ}}$ is representative of the distribution, while the arithmetic mean $\mathcal{L}_q^{\text{mean}}$ is not.

1. Multifractal exponents τ_q

We have so far considered q>1, but would obviously like to know the full q-dependence of τ_q for $q\geq 0$ and with arbitrary ξ . This can in fact be determined exactly within the framework employed. The basic reasons are as follows. Recall that τ_q is defined by Eq. 33, viz. $\tau_q=-\ln\mathcal{L}_q^{\rm typ}/\ln N$; and we want the finite limit of this as $L\to\infty$. So $\tau_q\equiv -\ln\mathcal{L}_q^{\rm typ}/(L\ln K)$, and from Eq. 26, $\ln\mathcal{L}_q^{\rm typ}\equiv \langle \ln\mathcal{L}_q(r_E)\rangle_{r_E}$ (such that e.g. $\langle r_E\rangle_{r_E}=L/2\rangle$. Now Eq. 27 gives the full expression for $\mathcal{N}^q\mathcal{L}_q(r_E)$, and in determining τ_q the normalisation factor \mathcal{N} plays no role $(\ln\mathcal{N}^q/L$ vanishes as $L\to\infty$). All that matters is which of the r_E -dependent exponentials appearing in Eq. 27 dominates the r_E sum in the expression for τ_q ; it being the logarithm of the dominant term(s) which determines τ_q as $L\to\infty$.

The upshot is that the q-dependence of τ_q depends on ξ and K solely in the combination $\xi \ln K$, and divides into two regimes: (a) For $\xi \ln K > 1$,

$$\tau_{q} = \begin{cases} (q-1) + \frac{q}{2\xi \ln K} &: 0 \le q \le q_{*}^{-} \\ \frac{1}{2}(q-1) &: q_{*}^{-} \le q \le q_{*}^{+} \\ \frac{q}{2\xi \ln K} &: q_{*}^{+} \le q \end{cases}$$
(38)

with $q_*^- < 1 < q_*^+$ given by

$$q_*^{\pm} = \frac{1}{1 \mp \frac{1}{\varepsilon \ln K}},\tag{39}$$

and with τ_q continuous as q crosses both q_*^- and q_*^+ . As $\xi \ln K \to 1+$, $q_*^+ \to \infty$, and the final regime in Eq. 38 is correspondingly absent. In this case: (b) For $\xi \ln K < 1$,

$$\tau_q = \begin{cases} (q-1) + \frac{q}{2\xi \ln K} &: 0 \le q \le q_*^- \\ \frac{1}{2}(q-1) &: q_*^- \le q \end{cases}$$
(40)

with τ_q again continuous as q crosses $q_*^- < 1$. As they must, Eqs. 38,40 recover the trivial limits $\tau_{q=1} = 0$ (from wavefunction normalisation) and $\tau_{q=0} = -1$.

For any fixed q, Eqs. 38,40 can of course be inverted, to give τ_q as a function of $\xi \ln K$. For $q \ge 1$ this yields

$$\tau_{q} = \begin{cases} \frac{1}{2}(q-1) & : 0 \le \xi \ln K \le \frac{q}{(q-1)} \\ \frac{q}{2\xi \ln K} & : \xi \ln K \ge \frac{q}{(q-1)} \end{cases}, (41)$$

while for any given $q \in [0, 1]$,

$$\tau_q = \begin{cases} \frac{1}{2}(q-1) & : 0 \le \xi \ln K \le \frac{q}{(1-q)} \\ (q-1) + \frac{q}{2\xi \ln K} & : \xi \ln K \ge \frac{q}{(1-q)} \end{cases} . (42)$$

The results above are illustrated in Fig. 4, which shows both the q-dependence of τ_q for three representative ξ 's (left panel), and its ξ -dependence for three representative q's (right panel). Eq. 38 for the q-dependence of τ_q , consisting as it does of three continuously connect regimes of linear q-dependence for $\xi \ln K > 1$, is exemplified by the $\xi = 3, 10$ examples; while the $\xi = 0.1$ example illustrates Eq. 40 (in this case, q_*^- is so small that only the $\tau_q = \frac{1}{2}(q-1)$ behaviour is shown).

Likewise, Eqs. 41,42 for the ξ -dependence of τ_q are exemplified in the right panel of Fig. 4. In particular, $\tau_q(\xi)$ for any given q is ξ -independent up to $\xi = \xi_c = q/(|q-1|\ln K)$, and decreases thereafter as ξ increases; whence $\mathcal{L}_q^{\mathrm{typ}} = N^{-\tau_q}$ increases with increasing ξ (i.e. decreasing disorder strength), which is the behaviour remarked upon in Fig. 3 above for $\ln \mathcal{L}_2^{\mathrm{typ}}$.

One further observation is worth noting here. For q < 1 the exponent τ_q is negative, corresponding to an $\mathcal{L}_q^{\mathrm{typ}} = N^{|\tau_q|} \propto e^{|\tau_q|L \ln K}$ which increases exponentially with the number of tree generations L. In that case, c_2 in Eq. 35 for $\mathcal{L}_q(r_E)$ is negative. The resultant $P_{\mathcal{L}_q}(\mathcal{L}_q)$, rather than being given by Eq. 36, is instead given by

$$P_{\mathcal{L}_q}(\mathcal{L}_q) = \frac{1}{\mathcal{L}_q} (|c_2|L)^{-1} \Theta(\mathcal{L}_q - c_1) \Theta(c_1 e^{|c_2|L} - \mathcal{L}_q)$$
(43)

with c_1 the lower limit, and the upper limit $c_1e^{|c_2|L}$ now exponentially large in L; such that the $\propto 1/\mathcal{L}_q$ fat tail in $P_{\mathcal{L}_q}(\mathcal{L}_q)$ extends up to exponentially large values of \mathcal{L}_q (albeit with exponentially small weight). The mean value of this distribution remains governed by its upper limit (as for q > 1), but $\mathcal{L}_q^{\text{mean}}$ is now exponentially large in L. As such, $\mathcal{L}_q^{\text{mean}}$ itself could legitimately be viewed as exhibiting multifractal behaviour (with a calculable exponent $\tilde{\tau}_q$). Yet this behaviour is particular to the q < 1 regime, and in marked contrast to all q > 1 where

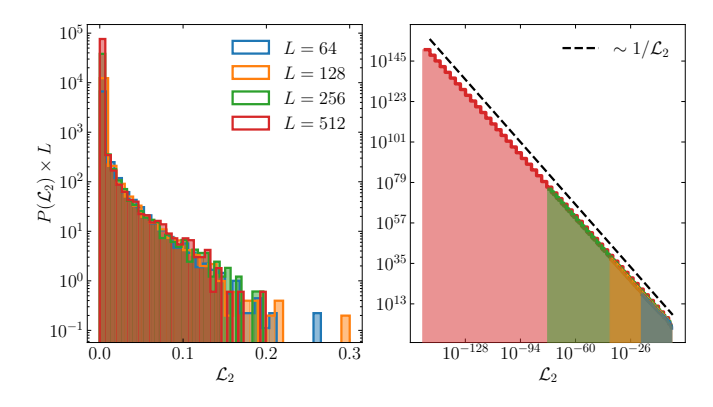


FIG. 5. Distribution $P_{\mathcal{L}_2}(\mathcal{L}_2)$ of \mathcal{L}_2 obtained from ED (shown for W=1 with K=2), for the number of generations L as indicated. For clarity, $L \times P_{\mathcal{L}_2}(\mathcal{L}_2)$ vs \mathcal{L}_2 is plotted (as explained in text). Left panel shows data with linear bins, right panel with logarithmic bins. In right panel, the black dashed line shows the $P_{\mathcal{L}_2}(\mathcal{L}_2) \propto 1/\mathcal{L}_2$ behaviour, Eq. 36.

 $\mathcal{L}_q^{\mathrm{mean}} \propto 1/L$ and multifractality does not arise in $\mathcal{L}_q^{\mathrm{mean}}$. It is only with the typical value $\mathcal{L}_q^{\mathrm{typ}}$ that robust multifractality arises for both q>1 and q<1; and which thus provides the appropriate touchstone for it.

D. Numerical results: Cayley tree

We now turn briefly to numerical calculations, obtained via exact diagonalisation (ED) on the 1d Krylov Hamiltonian Eq. 16. For the i.i.d. disorder in the $\{\mathcal{E}_r\}$, a box distribution $P_{\mathcal{E}}(\mathcal{E}) = (2W)^{-1}\Theta(W - |\mathcal{E}|)$ is taken. $\mathcal{L}_q(r_E)$ is calculated directly using Eq. 21, with the $\{|A_{E,r}|^2\}$ obtained from ED on the chain of length L. The calculations here extend up to $L \sim 500$, which corresponds for K=2 to a Cayley tree of ~ 500 generations and dimension $N \sim K^L \sim 10^{150}$. Results given below are averaged over ~ 2000 disorder realisations, and we also average over a substantial fraction of eigenstates in the band (which improves statistics and does not materially affect the results shown).

The analytically-based results of Sec. II C are well corroborated by ED. Fig. 5 shows the resultant ED distribution $P_{\mathcal{L}_2}(\mathcal{L}_2)$ of \mathcal{L}_2 (here illustrated by disorder strength W=1, with K=2). Since Eq. 36 gives $P_{\mathcal{L}_q}(\mathcal{L}_q) \propto 1/(\mathcal{L}_q L)$, we plot $L \times P_{\mathcal{L}_2}(\mathcal{L}_2)$ vs \mathcal{L}_2 , to expose cleanly the predicted power-law decay $P_{\mathcal{L}_2}(\mathcal{L}_2) \propto 1/\mathcal{L}_2$; and which behaviour is clearly seen in Fig. 5.

Fig. 6 shows ED results for $\mathcal{L}_2^{\text{mean}}$ vs L and $\mathcal{L}_2^{\text{typ}}$ vs $N \propto K^L$, for the range of disorder strengths W indicated. These indeed confirm that $\mathcal{L}_2^{\text{mean}} \propto 1/L$, with

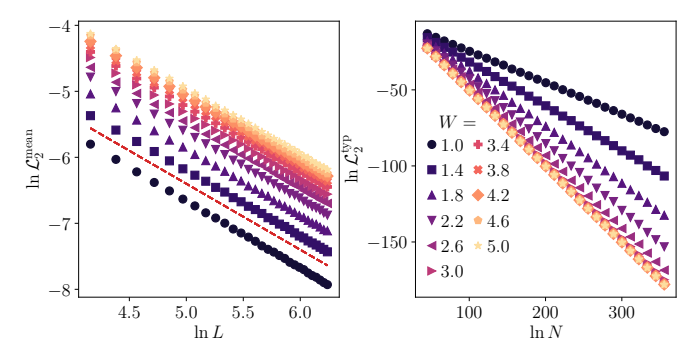


FIG. 6. Mean $\mathcal{L}_2^{\text{mean}}$ (left) and typical $\mathcal{L}_2^{\text{typ}}$ (right) IPR obtained numerically from ED for different disorder strengths W (with K=2). $\mathcal{L}_2^{\text{mean}}$ is plotted against the total number of tree generations, L, whereas $\mathcal{L}_2^{\text{typ}}$ is plotted against the total number of sites on the tree, $N \propto K^L$ (Eq. 30). Red dashed line in left panel for $\mathcal{L}_2^{\text{mean}}$ indicates a slope of -1.

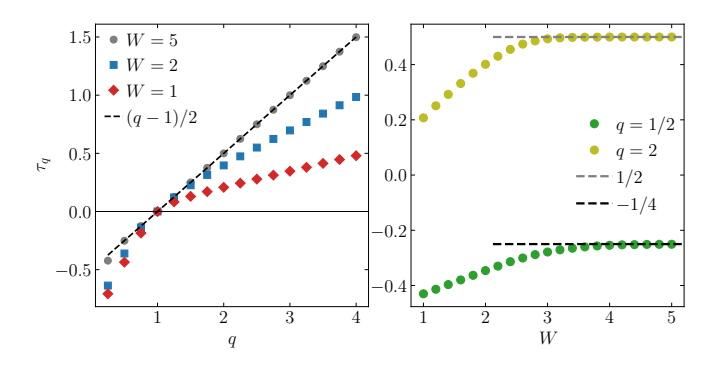


FIG. 7. ED results for multifractal exponents τ_q . Left panel: τ_q vs q for disorder strengths W=1,2,5. Black dashed line shows $\frac{1}{2}(q-1)$. Corresponding analytical results for different ξ are shown in Fig. 4 (left panel). Discussion in text. Right panel: τ_q vs W, shown for q=2 and 1/2. Dashed lines show the asymptotes $\frac{1}{2}(q-1)$. For comparison, analytical results for τ_q vs ξ are shown in Fig. 4 (right panel).

an overall magnitude that increases with increasing W (\equiv decreasing ξ); and that $\mathcal{L}_2^{\mathrm{typ}} \propto N^{-\tau_2}$ with a fractal exponent τ_2 which increases with increasing W. These results should be compared to their analytical counterparts shown in Fig. 3, where the same quantities were plotted for a range of ξ , remembering that the effective ξ will decrease with increasing W. While there is naturally no direct mapping between the disorder strength W, and ξ appearing in the analytical treatment, the agreement between the two is self-evident.

Fig. 7 pursues further the behaviour of the multifractal exponents τ_q obtained from ED. As in Fig. 6 for q=2, plots of $\ln \mathcal{L}_q^{\rm typ}$ $vs \ln N$ are found to show pristine linearity for any q, enabling $\tau_q=-\ln \mathcal{L}_q^{\rm typ}/\ln N$ to be read off. For q=2 and 1/2, the right panel of Fig. 7 shows the evolution of the resultant τ_q as a function of W; analytical results for the ξ -dependence of τ_q are given in Fig. 4 (right panel). Given that the effective ξ decreases with increasing W, the agreement between

³ As far as ED on the 1d Krylov chain is concerned, it is of course straightforward to go to much larger values of L; but the smallness of terms in the r-sum in Eq. 21 for \mathcal{L}_q then requires careful handling, and for our purposes there is little gain in doing so.

the two is evident. In particular, the large-W behaviour $\tau_q = \frac{1}{2}(q-1)$ obtained via ED is precisely that arising from the small- ξ analytical results (Eqs. 41,42).

ED results for τ_q vs q are shown in the left panel of Fig. 7, for W=1,2,5; corresponding analytical results for different ξ 's are shown in Fig. 4 (left panel). For strong disorder, W=5, the ED results indeed show the behaviour $\tau_q=\frac{1}{2}(q-1)$ over the wide q-range shown, just as they do for the $\xi=0.1$ case in the left panel of Fig. 4 (as per Eqs. 40). And for weaker disorder, e.g. W=2, one sees three regimes of linear q-dependence, as arises for e.g. the $\xi=3$ case shown in the left panel of Fig. 4 (and reflecting Eq. 38).

III. RADIAL AUBRY-ANDRÉ TREE

Quenched disorder is not of course the only mechanism that can induce localisation: incommensurability is another, see e.g. [72, 77–86]. We consider now what we refer to as a radial Aubry-André (AA) model. Again, the site-energies for sites r_n on the Cayley tree satisfy $\mathcal{E}_{r_n} = \mathcal{E}_r$ independent of the particular sites n on row/generation r. In this case they are given by the AA potential [72] $\mathcal{E}_r = V \cos(2\pi\kappa r + \phi)$, with κ an irrational – chosen for ED calculations as $\Phi - 1$ with Φ the golden mean – and ϕ a random phase (averaging over which is the analogue of disorder averaging). In the totally symmetric basis $\{|\tilde{r}_1\rangle\}$ (Eq. 10), the associated 1d Krylov Hamiltonian $\hat{\mathcal{H}}$ again has precisely the form Eq. 16.

In contrast to 1d problems with uncorrelated quenched disorder, the 1d AA model possesses a transition between a delocalised and a localised phase [72]. By a familiar duality argument [72], this occurs when the potential strength V is precisely twice the magnitude of the hopping matrix element; so for Eq. 16 the critical $V_c = 2\sqrt{K}\Gamma$. For $V > V_c$, all states are exponentially localised, while for $V < V_c$ all eigenstates are delocalised (there being no mobility edge in the AA model).

A. Analytical considerations

Consider first the behaviour of the system in the localised phase of the 1d model, $V > V_{\rm c} = 2\sqrt{K}\Gamma$. Here, as a function of the localisation length ξ , the properties of the system are again just as given in Sec. II C. The difference in the present case is of course that ξ diverges as V approaches from above the *finite* $V_{\rm c}$ at which the transition occurs. The form of that divergence is known exactly [78], $\xi \propto (V - V_{\rm c})^{-1}$.

The IPRs \mathcal{L}_q in the original tree basis remain given by Eq. 21. As a function of ξ , their properties are just as determined in Secs. II C, II C 1; and the points made about them there hold equally here. In this regime multifractality is ubiquitous, and two points about the behaviour of the IPR exponent τ_q should be noted. First, sufficiently deep in the multifractal phase where $\xi \ll 1$, the

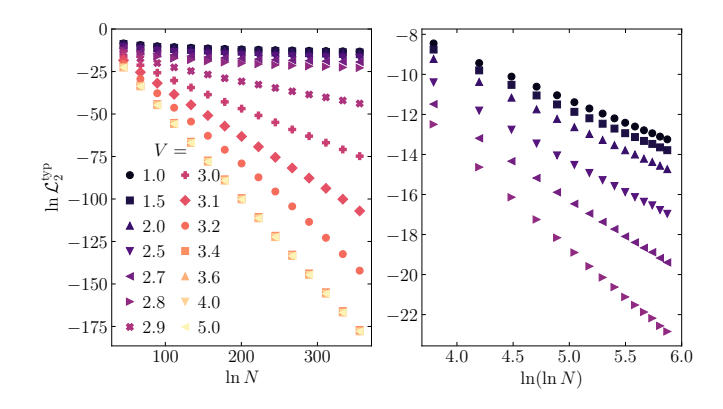


FIG. 8. Radial AA tree. The ϕ -averaged typical IPR $\ln \mathcal{L}_2^{\mathrm{typ}}$ is shown for the range of V indicated, with K=2. Left panel shows $\ln \mathcal{L}_2^{\mathrm{typ}}$ $vs \ln N \propto L$. Right panel shows $\ln \mathcal{L}_2^{\mathrm{typ}}$ $vs \ln(\ln N) \propto \ln L$, for values of $V < V_{\mathrm{c}}$ ($V_{\mathrm{c}} = 2\sqrt{K} \simeq 2.8$ for K=2). $\Gamma \equiv 1$ is taken. Discussion in text.

behaviour $\tau_q = \frac{1}{2}(q-1)$ (Eqs. 34,41,42) will again arise; as too will the behaviour $\tau_q \propto 1/\xi$ for $\xi \gg 1$ and any q > 1 (Eq. 41). Second, since $1/\xi \propto (V-V_c)$, the latter implies

$$\tau_q \stackrel{V \to V_c +}{\sim} (V - V_c) \qquad : V_c = 2\sqrt{K}\Gamma .$$
 (44)

 τ_q must thus vanish on approach to the transition from the multifractal/localised side, with a critical exponent of 1 (from Eq. 42, the analogue of this for any $q \in (0,1)$ is $\tau_q - (q-1) \sim (V-V_c)$ as $V \to V_c+$).

For $V < V_c$, the 1d model has a delocalised phase (of which there is no counterpart in the radially disordered tree of the previous sections). Here we can say relatively little a priori, save for deep in the small- $V \ll V_c$ regime where essentially uniform delocalisation is expected, with $|A_{E,r}|^2 \simeq 1/L$ for all r. $\mathcal{L}_q(r_E)$ then follows from Eq. 21 (with $N_r = K^r$), and does not depend on r_E . So from Eq. 26, $\mathcal{L}_q^{\text{typ}} \equiv \mathcal{L}_q^{\text{mean}}$ – here denoted simply by \mathcal{L}_q – follows for any q > 1 (on which we focus in the following) as

$$\mathcal{L}_q \stackrel{V \to 0}{\sim} \frac{1}{[1 - K^{-(q-1)}]} \times \frac{1}{L^q} ;$$
 (45)

which we examine numerically below. Let us also remark here that this $V \to 0$ L-dependence, $\mathcal{L}_q \sim L^{-q}$, is unsurprisingly different from that of the IPR $L_q = \sum_{r=0}^{L} |A_{E,r}|^{2q}$ in the 1d \tilde{r}_1 -basis; which, with $|A_{E,r}|^2 \simeq 1/L$, instead gives $L_q \sim L^{-(q-1)}$.

B. Numerical results: radial AA tree

We turn now to numerical results obtained via ED (with data averaged over randomly chosen values of $\phi \in [0, \pi]$).

The left panel in Fig. 8 shows $\ln \mathcal{L}_2^{\rm typ}$ vs $\ln N \ (\propto L)$, for K=2. The critical $V_{\rm c}=2\sqrt{K}\simeq 2.8$ (taking $\Gamma\equiv 1$). From this it is seen that for $V>V_{\rm c}$, clear multifractal

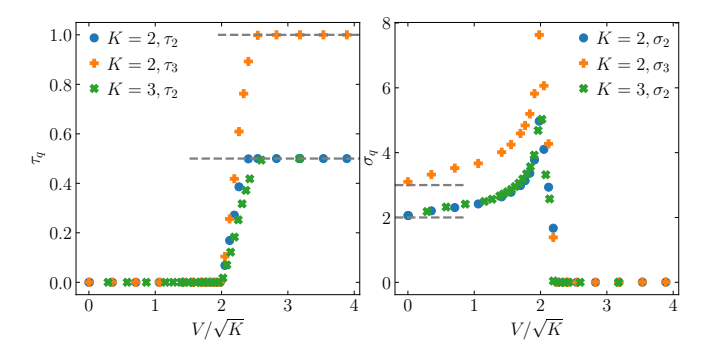


FIG. 9. Radial AA tree. Left panel: multifractal exponent τ_q vs V/\sqrt{K} ($\Gamma\equiv 1$), shown for q=2,3 and K=2,3, as indicated. In all cases, $\tau_q\propto (V-V_c)$ vanishes linearly as $V\to V_c+$, with the K-independent $V_c/\sqrt{K}=2$. Dashed lines denote the large-V asymptotic behaviour $\tau_q=\frac{1}{2}(q-1)$ (Eq. 41). Right panel: σ_q vs V/\sqrt{K} for q,K as indicated; showing $\sigma_q\to q$ as $V\to 0$ (dashed lines).

behaviour $\mathcal{L}_2^{\mathrm{typ}} \propto N^{-\tau_2}$ indeed arises; and that τ_2 in practice saturates by $V \simeq 3.4$, only modestly in excess of the critical V_{c} .

For $V < V_c$ by contrast, $\ln \mathcal{L}_2^{\mathrm{typ}}$ in Fig. 8 (left panel) appears scarcely to depend on N. What is occurring in this regime is evident in the right panel of Fig. 8, where $\ln \mathcal{L}_2^{\mathrm{typ}}$ is instead plotted $vs \ln(\ln N) \propto \ln L$. These plots are clearly linear, indicating the form $\mathcal{L}_2^{\mathrm{typ}} \propto L^{-\sigma_2}$; and which behaviour is consistent with the argument above, giving $\mathcal{L}_2 \propto L^{-2}$ as $V \to 0$ (Eq. 45).

To examine the transition between the two distinct behaviours arising for $V \geq V_c$, we fit the ED data to the form

$$\ln \mathcal{L}_q^{\text{typ}} = -\tau_q \ln N - \sigma_q \ln \ln N + c_q. \tag{46}$$

The outcome of this is shown in Fig. 9 where, for q=2,3, the resultant τ_q and σ_q are shown as a function of $V/(\sqrt{K}\Gamma)$ ($\Gamma\equiv 1$). These are given for both K=2,3 as indicated, such that the transition should occur for $V/\sqrt{K}=2$ in either case; which it evidently does. The following points should be noted:

- 1. For the multifractal phase, τ_q agrees well with the analytic results of Sec. III A. It is indeed seen to saturate for large V/\sqrt{K} to the predicted value $\tau_q = \frac{1}{2}(q-1)$ (Eq. 41). τ_q decreases with decreasing V, vanishes on approach to the transition from the multifractal phase $V \to V_c+$, and does so linearly in $(V-V_c)$, in accordance with Eq. 44.
- 2. For $V < V_c$ $(V/\sqrt{K} < 2)$ by contrast, $\tau_q = 0$. So in this regime one has the behaviour

$$\mathcal{L}_q^{\mathrm{typ}} \sim \left(\ln N \right)^{-\sigma_q} \propto L^{-\sigma_q} : V < V_{\mathrm{c}},$$
 (47)

as seen explicitly in Fig. 8 (right panel) for q=2. This is consistent with the deduction in Eq. 45 that $\mathcal{L}_q^{\mathrm{typ}} \propto L^{-q}$ as $V \to 0$, and from Fig. 9 $\sigma_q \to q$ as

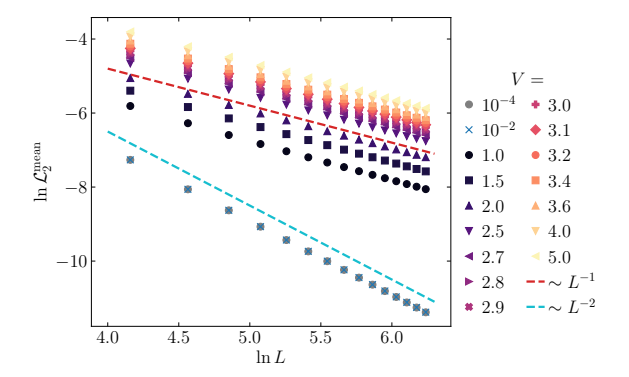


FIG. 10. Radial AA tree. Mean IPR (for q=2 and K=2), shown as $\ln \mathcal{L}_2^{\rm mean}$ vs $\ln L$, for the wide range of V indicated. For the smallest $V \ll V_c$ shown, $\mathcal{L}_2^{\rm mean} \propto L^{-2}$, in accordance with Eq. 45 (the data for $V=10^{-4}$ and 10^{-2} are indistinguishable); the blue dashed line indicating a slope of -2. For larger V by contrast, $\mathcal{L}_2^{\rm mean} \propto L^{-1}$ is found, the slope of -1 being indicated by the red dashed line.

 $V \to 0$ is indeed seen to arise. On increasing V, the σ_q (Fig. 9 right) are seen to increase steadily as V approaches V_c , then sharply (but we believe continuously) decrease in the multifractal phase above V_c (where τ_q itself is non-zero), to an essentially negligible value for V very slightly in excess of V_c .

We add that the $V < V_c$ behaviour of $\mathcal{L}_q^{\mathrm{typ}}$ (Eq. 47) is an unusually weak form of multifractality, scaling as it does with a power of $\ln N$ (rather than a power of N, as in the multifractal phase $V > V_c$).

Finally, while our natural focus above has been on the typical IPR, we comment briefly on the mean IPR; as illustrated in Fig. 10, where $\ln \mathcal{L}_2^{\text{mean}}$ is shown as a function of $\ln L$ for a wide range of V. Writing $\mathcal{L}_2^{\text{mean}} \propto L^{-\sigma_2'}$, Eq. 45 indeed holds for the very smallest values of $V \ll V_{\rm c}$, namely $\sigma_2' = 2 = q$ (with the distribution of \mathcal{L}_2 sufficiently narrow that its mean and typical values are essentially the same). This is evident in Fig. 10 for the two lowest V shown, $V = 10^{-4}$ and 10^{-2} . But on increasing V further – still deep in the delocalised regime $V \ll V_{\rm c}$ – the distribution of \mathcal{L}_2 broadens such that $\mathcal{L}_2^{\mathrm{mean}}$ and $\mathcal{L}_{2}^{\mathrm{typ}}$ differ appreciably; and σ_{2}' rapidly crosses over with increasing V to $\sigma_2' = 1$. It remains at this value across the transition at $V = V_c$, and throughout the multifractal phase (as known from the considerations of Sec. II). As such, and in marked contrast to the typical $\mathcal{L}_{q}^{\text{typ}}$, the behaviour of $\mathcal{L}_q^{\text{mean}}$ is in essence 'blind' to the transition, reflecting the atypicality of the mean IPR as a measure of its distribution, as discussed extensively in Sec. II.

IV. HYPERCUBE GRAPH

So far we have considered Cayley trees, with radial disorder or analogous incommensurability. Now we turn to the L-dimensional hypercube graph (see Fig. 2), the

essential properties of which have been summarised in Sec. I A.

Before proceeding, let us recall one example of the TBM (Eq. 1) on this graph [25]; namely the random energy limit, in which all $N=2^L$ site energies $\{\mathcal{E}_i\}$ are treated as completely uncorrelated i.i.d. random variables (with an N-dependent variance chosen to match that of the density of states). This is an example of a quantum random energy model, the states of which are known to be invariably delocalised/ergodic [25, 70, 71]. Such behaviour is almost the antithesis of the radial disorder considered here, underscoring the key role correlations in the $\{\mathcal{E}_i\}$ may play.

As for the Cayley tree of Sec. II, we look first at the case $\hat{H}_0 \equiv 0$, so that $\hat{H} \equiv \hat{H}_{\Gamma}$ involves solely the hopping parts of the TBM. We first show that, as for the tree (Sec. IIB), only the totally symmetric combination $\{|\tilde{r}_1\rangle\}$ of orbitals – again given by Eq. 10, now with $N_r = {L \choose r}$ – are connected under \hat{H}_{Γ} starting from the apical 'root' site $|0\rangle$ of the graph.

As the topology of the hypercube is quite different from that of a tree, this is not entirely obvious at first sight. To show it, it is convenient to split \hat{H}_{Γ} (Eq. 1) into $\hat{H}_{\Gamma} = \hat{H}_{\Gamma}^+ + \hat{H}_{\Gamma}^-$, where \hat{H}_{Γ}^\pm connects any basis state $|r_n\rangle$ in row r to states in rows $r\pm 1$ respectively. Consider $\hat{H}_{\Gamma}^+ \sum_{n=1}^{N_r} |r_n\rangle$. As noted in Sec. IA, each $|r_n\rangle$ connects under \hat{H}_{Γ}^+ to (L-r) distinct basis states $|(r+1)_n\rangle$, and each such $|(r+1)_n\rangle$ occurs (r+1) times in $\hat{H}_{\Gamma}^+ \sum_{n=1}^{N_r} |r_n\rangle$; so $\hat{H}_{\Gamma}^+ \sum_{n=1}^{N_r} |r_n\rangle = \Gamma(r+1) \sum_{n=1}^{N_{r+1}} |(r+1)_n\rangle$. By the same token, each $|r_n\rangle$ connects under \hat{H}_{Γ}^- to r distinct basis states $|(r-1)_n\rangle$, and each such state occurs (L-[r-1]) times in $\hat{H}_{\Gamma}^- \sum_{n=1}^{N_r} |r_n\rangle$, so $\hat{H}_{\Gamma}^- \sum_{n=1}^{N_r} |r_n\rangle = \Gamma(L-[r-1]) \sum_{n=1}^{N_{r-1}} |(r-1)_n\rangle$. From these, $\hat{H}_{\Gamma} \sum_{n=1}^{N_r} |r_n\rangle$ follows. Using the definition $|\tilde{r}_1\rangle = N_r^{-1/2} \sum_{n=1}^{N_r} |r_n\rangle$ (Eq. 10) of the totally symmetric $|\tilde{r}_1\rangle$ then gives

$$\hat{H}_{\Gamma}|\tilde{r}_{1}\rangle = \Gamma\sqrt{r(L-[r-1])} |(\widetilde{r-1})_{1}\rangle
+ \Gamma\sqrt{(r+1)(L-r)} |(\widetilde{r+1})_{1}\rangle;$$
(48)

holding for any $r=0,1,\cdots L$ (and with $|\tilde{0}_1\rangle=|0\rangle$ the apex orbital). Solely the totally symmetric linear combinations of basis states on any row of the hypercube graph are thus indeed coupled under \hat{H}_{Γ} , starting from $|0\rangle$.

Comparison to Eq. 15 in turn shows Eq. 48 to be precisely the tridiagonal Krylov Hamiltonian, with Krylov basis $|k_r\rangle = |\tilde{r}_1\rangle$ generated under $\hat{H} \equiv \hat{H}_{\Gamma}$ from $|k_0\rangle = |0\rangle$; and with $b_r = \Gamma \sqrt{r(L - [r - 1])}$ and $a_r = 0$. As for the Cayley tree the hypercube graph thus fragments and, to be consistent with the notation of Sec. II, we denote by $\hat{\mathcal{H}}_{\Gamma}$ the Krylov Hamiltonian in the basis $\mathcal{K}(\hat{H}, |0\rangle) = \text{span}\{|\tilde{r}_1\rangle : r = 0, 1, 2, \cdots L\}$, viz.

$$\hat{\mathcal{H}}_{\Gamma} = \Gamma \sum_{r=1}^{L} \left(\sqrt{r(L - [r-1])} | \widetilde{(r-1)}_{1} \rangle \langle \tilde{r}_{1} | + \text{h.c.} \right). \tag{49}$$

For use below, let us comment briefly on the density of states (DoS) of this tridiagonal \mathcal{H}_{Γ} ; denoted by

 $D_{\Gamma}(\omega)$ (and normalised such that $\int d\omega \ D_{\Gamma}(\omega) = 1$). The properties of $D_{\Gamma}(\omega)$ we want can be obtained in several ways, but here it suffices to use a result from [74] which relates the DoS to the Lanczos coefficients $b_r = \Gamma \sqrt{r(L - [r - 1])}$. Defining x = r/L ($\in [0, 1]$), and regarding $b(x) \equiv b_{r=xL}$ as a continuous function of x as $L \to \infty$, then [74]

$$D_{\Gamma}(\omega) = \int_0^1 dx \, \frac{\Theta(4b^2(x) - \omega^2)}{\pi \sqrt{4b^2(x) - \omega^2}}.$$
 (50)

In the present case $b(x) \equiv L\Gamma x(1-x)$, and evaluation of Eq. 50 gives

$$D_{\Gamma}(\omega) = \frac{\Theta(\Gamma L - |\omega|)}{2\Gamma L},\tag{51}$$

which has a full width $2\Gamma L$, a vanishing mean and a variance $\int d\omega \ \omega^2 D_{\Gamma}(\omega) = \frac{1}{3}\Gamma^2 L^2 \propto L^2.4$

Now consider the effect of \hat{H}_0 . As for the Cayley tree, this is expressible in the row-resolved form Eq. 2. And by the same argument given at the start of Sec. II B, the fragmentation arising under \hat{H}_{Γ} alone persists in the presence of radial disorder $(\mathcal{E}_{r_n} = \mathcal{E}_r)$. In particular, the separable part of the Hamiltonian which contains the root site, again denoted by $\hat{\mathcal{H}} = \hat{\mathcal{H}}_0 + \hat{\mathcal{H}}_{\Gamma}$, is

$$\hat{\mathcal{H}} = \sum_{r=0}^{L} \mathcal{E}_r |\tilde{r}_1\rangle \langle \tilde{r}_1| + \hat{\mathcal{H}}_{\Gamma}.$$
 (52)

This is the full Krylov Hamiltonian, on which we focus (now with $a_r = \mathcal{E}_r$ and $b_r = \Gamma \sqrt{r(L - [r - 1])}$.

As for the tree case, we consider the L+1 site-energies $\{\mathcal{E}_r\}$ to be independent random variables. Since, as above, the hoppings in $\hat{\mathcal{H}}_{\Gamma}$ generate a spectral density $D_{\Gamma}(\omega)$ whose variance is $\propto L^2$, then to ensure the hopping $\hat{\mathcal{H}}_{\Gamma}$ does not trivially overwhelm the disorder as $L \to \infty$, the distribution $P_{\mathcal{E}_r}(\mathcal{E}_r)$ of \mathcal{E}_r must have a variance which essentially matches this behaviour. While there are many possible choices for this, for our ED calculations (Sec. IVB) we consider in practice the distribution $P_{\mathcal{E}_r}(\mathcal{E}_r)$ to be normal, with zero mean and a variance of $W^2r(L-[r-1]) \equiv W^2L^2x(1-x)$ (the r-dependence of which matches that of the hoppings b_r^2). With this, we expect (and find) exponential localisation in the \tilde{r}_1 -basis for non-zero disorder strengths W; i.e., just as in Eq. 22, $|A_{E,r}|^2 = \mathcal{N}^{-1} \exp(-|r - r_E|/\xi)$, with localisation centre r_E and localisation length ξ . Given this, without regard to the precise form of the disorder distribution, we can of course proceed to analytical considerations analogous to those given in Sec. II C for the tree graph.

⁴ We add that Eq. 50 also encompasses $D_{\Gamma}(\omega)$ for the Krylov $\hat{\mathcal{H}}_{\Gamma}$ (Eq. 11) arising for the tree as $L \to \infty$. In that case, $b_r = \sqrt{K}\Gamma$ is r-independent (Sec. II A 1), so $b(x) = \sqrt{K}\Gamma$ is x-independent. Eq. 50 then (trivially) yields precisely the DoS of an infinite 1d chain with a nearest neighbour hopping of $\sqrt{K}\Gamma$ [87]; as it should by the arguments given in Sec. II A.

A. Analytical considerations

In considering the hypercube, we will focus for brevity on $q \geq 1$. Note also that Eqs. 17-21 of Sec. IIB again hold, now with the number of sites on row r of the graph given by $N_r = {L \choose r}$. In particular, the IPRs in the original hypercube basis are given by Eq. 21; i.e. with Eq. 22 for $|A_{E,r}|^2$,

$$\mathcal{N}^{q} \mathcal{L}_{q}(r_{E}) = \sum_{r=0}^{L} \frac{1}{\binom{L}{r}^{(q-1)}} e^{-q|r-r_{E}|/\xi}.$$
 (53)

Separating this r-sum into $r < r_E$ and $r > r_E$, and using $\binom{L}{r} = \binom{L}{L-r}$, shows the physically obvious symmetry

$$\mathcal{L}_q(r_E) = \mathcal{L}_q(L - r_E). \tag{54}$$

Only $r_E \leq L/2$ need then be considered, with the typical and mean values of the distribution $P_{\mathcal{L}_q}(\mathcal{L}_q)$ given from Eq. 26 as

$$\ln \mathcal{L}_{q}^{\text{typ}} = \frac{1}{L+1} \left[2 \sum_{r_{E}=0}^{\frac{L}{2}} \ln \mathcal{L}_{q}(r_{E}) - \ln \mathcal{L}_{q}\left(\frac{L}{2}\right) \right]$$

$$\mathcal{L}_{q}^{\text{mean}} = \frac{1}{L+1} \left[2 \sum_{r_{E}=0}^{\frac{L}{2}} \mathcal{L}_{q}(r_{E}) - \mathcal{L}_{q}\left(\frac{L}{2}\right) \right].$$
(55)

In parallel to Sec. II C for the tree, let us first look at this in the two cases of $\xi \ll 1$ and $\xi \gg 1$, again considering r_E to be $\propto L$ with probability unity. For $\xi \ll 1$, Eq. 53 is asymptotically dominated by the term with $r = r_E$, so

$$\mathcal{L}_{q}(r_{E}) \overset{\xi \ll 1}{\sim} \begin{pmatrix} L \\ r_{E} \end{pmatrix}^{-(q-1)} \tag{56}$$

(using also $\mathcal{N} \sim 1$ for $\xi \ll 1$, see Eq. 24). For $\xi \gg 1$ by contrast (and with $r_E \leq L/2$), the r=0 term in Eq. 53 dominates, to give

$$\mathcal{N}^q \mathcal{L}_q(r_E) \stackrel{\xi \gg 1}{\sim} e^{-qr_E/\xi}$$
 (57)

(with $\mathcal{N} \sim 2\xi$ in this case).

Using the full Eq. 53 for $\mathcal{L}_q(r_E)$, together with Eq. 55, Fig. 11 shows the mean and typical IPRs for q=2 over a wide range of ξ ; with $\mathcal{L}_2^{\text{mean}}$ shown as a function of L and $\mathcal{L}_2^{\text{typ}}$ as a function of the total number of sites on the graph, $N=2^L$. Precisely the same three qualitative features stand out as were apparent in Fig. 3 for the Cayley tree: that $\mathcal{L}_2^{\text{mean}} \propto 1/L$; that $\mathcal{L}_2^{\text{typ}}$ is many orders of magnitude smaller than $\mathcal{L}_2^{\text{mean}}$; and that $\mathcal{L}_2^{\text{typ}} \propto N^{-\tau_2}$ where the multifractal exponent τ_2 decreases with increasing ξ (i.e. decreasing disorder).

To understand these features, we again analyse the behaviour in the two limits of large and small ξ . First, consider $\mathcal{L}_q^{\text{mean}}$. For $\xi \ll 1$, Eq. 56 used in Eq. 55 shows that the latter sum is dominated by $r_E = 0$ for $L \gg 1$, giving

$$\mathcal{L}_q^{\text{mean}} \overset{L \gg 1}{\sim} \frac{2}{L} : \xi \ll 1.$$
 (58)

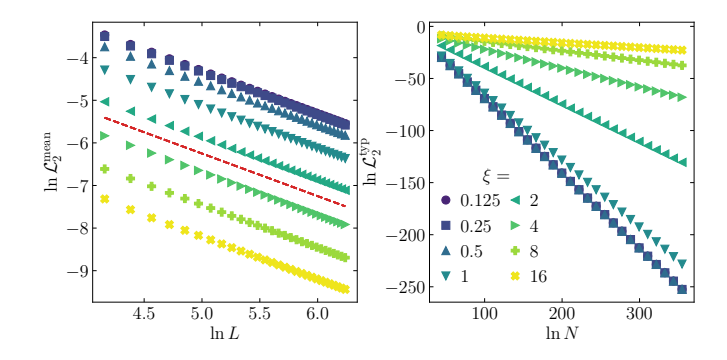


FIG. 11. Hypercube graph. Mean $\mathcal{L}_2^{\text{mean}}$ (left) and typical $\mathcal{L}_2^{\text{typ}}$ (right) IPR for q=2, computed from the full analytical expressions Eqs. 53,55, for the range of ξ indicated. $\ln \mathcal{L}_2^{\text{mean}}$ is plotted $vs \ln L$, while $\ln \mathcal{L}_2^{\text{typ}}$ is plotted against $\ln N = L \ln 2$. Red dashed line in the $\ln \mathcal{L}_2^{\text{mean}}$ plot indicates a slope of -1.

For $\xi \gg 1$, Eqs. 57,55 correspondingly give

$$\mathcal{L}_q^{\text{mean}} \overset{L \gg 1}{\sim} \frac{1}{q(2\xi)^{q-1}} \frac{1}{L} \qquad : \xi \gg 1. \tag{59}$$

So just as for the Cayley tree, whether $\xi\gg 1$ or $\xi\ll 1$, one indeed finds $\mathcal{L}_q^{\rm mean}\propto 1/L$.

Now turn to $\mathcal{L}_q^{\text{typ}}$, considering first $\xi \gg 1$ for which Eqs. 57,55 give

$$\mathcal{L}_q^{\text{typ}} \stackrel{L\gg 1}{\sim} \frac{1}{(2\xi)^q} \exp\left[-\frac{qL}{4\xi}\right] \sim N^{-\frac{q}{4\xi \ln 2}} : \xi \gg 1 \tag{60}$$

with the power-law decay in N reflecting multifractality. From the definition of the multifractal exponent (Eq. 33), $\tau_q = -\ln \mathcal{L}_q^{\rm typ} / \ln N$, so

$$\tau_q = \frac{q}{4\xi \ln 2} : \xi \gg 1. \tag{61}$$

For $\xi \ll 1$, Eq. 56 used in Eq. 55 gives

$$\ln \mathcal{L}_q^{\text{typ}} \stackrel{\xi \ll 1}{\sim} - \frac{(q-1)}{L+1} \sum_{r_E=0}^L \ln \binom{L}{r_E}$$

$$= -\frac{(q-1)}{L+1} \ln \left[\frac{\left(\Gamma(1+L)\right)^L}{G(1+L)G(2+L)} \right]$$
(62)

with G(z) the Barnes G-function; from the large-L asymptotics of which $\tau_q = -\ln \mathcal{L}_q^{\text{typ}}/L \ln 2$ follows as

$$\tau_q = \frac{(q-1)}{2\ln 2} \left[1 - \frac{\ln L}{L} + \mathcal{O}(L^{-1}) \right] \quad : \; \xi \ll 1. \quad (63)$$

Eqs. 61,63 for $\tau_q(\xi)$ have of course been obtained asymptotically, for large- and small- ξ . As with their counterparts for the Cayley tree (Sec. II C 1), however, and for the same basic reasons, the τ_q for $L \to \infty$ can be determined exactly within the framework employed. We first simply state the outcome of the latter, before returning to Eqs. 61,63.

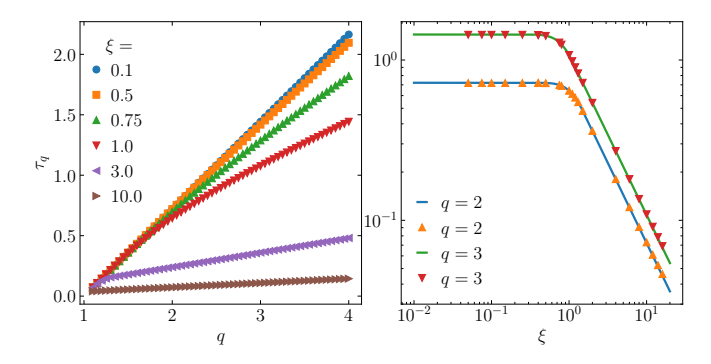


FIG. 12. Hypercube graph. Multifractal exponents τ_q , given by Eqs. 64,65. Left panel: τ_q vs q, shown for the range of ξ indicated. Right panel: τ_q vs ξ , shown for q=2 and 3. The small- ξ asymptote $\tau_q=(q-1)/(2\ln 2)$ (Eq. 63) is evident, as is the behaviour $\tau_q=q/(4\xi\ln 2)$ occurring for all $\xi\geq \xi_c$ (Eq. 64). Solid lines denote results from Eqs. 64,65 (which are exact as $L\to\infty$); points show $\tau_q=-\ln \mathcal{L}_q^{\rm typ}/L\ln 2$ calculated numerically using Eqs. 53,55 for L=512.

1. Multifractal exponents τ_q

For $\xi \geq \xi_c$, τ_q as a function of ξ is given by

$$\tau_q = \frac{q}{4\xi \ln 2} \quad : \xi \ge \xi_c := \frac{q}{(q-1)2 \ln 2}$$
(64)

(with ξ_c thus defined). This is the large- ξ form Eq. 61 again, but in fact holds for all $\xi \geq \xi_c$. For $\xi \leq \xi_c$, the ξ -dependence of τ_q is given for any chosen q > 1 by solution of the parametric equations

$$\tau_q = \frac{(q-1)}{\ln 2} \left[\frac{1}{2} - y - (1-y) \ln(1-y) \right] \tag{65a}$$

$$\xi = -\frac{q}{(q-1)} \left[\ln y + \left(\frac{1}{y} - 1 \right) \ln(1-y) \right]^{-1}$$
 (65b)

with y in the interval $[0,\frac{1}{2}]$. As $y \to \frac{1}{2}-$, one sees that $\xi \to \xi_c-$ and $\tau_q(\xi) \to q/(4\xi_c \ln 2)$ ($\equiv (q-1)/2$) thus connects continuously to Eq. 64. $\tau_q(\xi)$ increases continuously with decreasing $\xi < \xi_c$, which corresponds to y < 1/2 in Eqs. 65. In particular, $y \ll 1/2$ corresponds to $\xi \ll \xi_c$, for which Eq. 65a gives $\tau_q \to (q-1)/(2\ln 2)$ – indeed recovering Eq. 63.

These same equations naturally determine the q-dependence of τ_q for some given ξ . Eq. 64 holds for all $q \geq q_* := [1 - \frac{1}{2\xi \ln 2}]^{-1}$, which necessitates $2\xi \ln 2 > 1$. For $q \leq q_*$ (and any chosen ξ), τ_q is again determined parametrically by Eqs. 65. Note also that as $q \to 1$, Eqs. 65 are governed by $y \to 0$, Eq. 65a yielding $\tau_q \to (q-1)/(2\ln 2)$ independently of ξ (and recovering correctly $\tau_1 = 0$, as mandated trivially by wavefunction normalisation).

The results above are exemplified in Fig. 12, the right panel of which shows the ξ -dependence of τ_q for q=2 and q=3. Solid lines show the requisite $L\to\infty$ results from Eqs. 64,65, while points show $\tau_q=-\ln\mathcal{L}_q^{\rm typ}/L\ln 2$ calculated numerically using Eqs. 53,55 for L=512. As

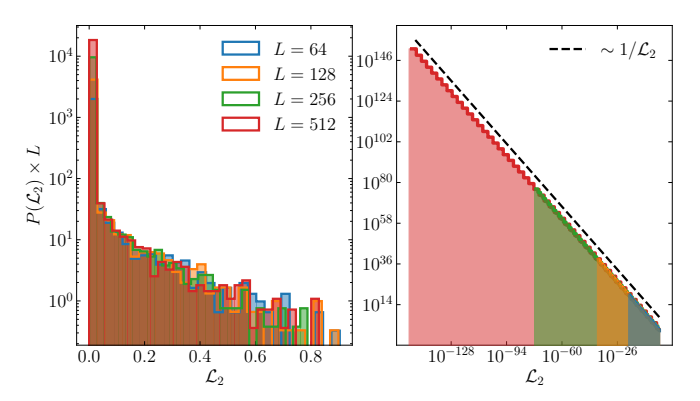


FIG. 13. Distribution $P_{\mathcal{L}_2}(\mathcal{L}_2)$ of \mathcal{L}_2 for the hypercube graph, obtained from ED (with W=1), for the linear system sizes indicated (with $N=2^L$). Just as in Fig. 5 for the tree, $L \times P_{\mathcal{L}_2}(\mathcal{L}_2)$ vs \mathcal{L}_2 is plotted. Left panel shows data with linear bins, right panel with logarithmic bins. In right panel, the black dashed line shows the $P_{\mathcal{L}_2}(\mathcal{L}_2) \propto 1/\mathcal{L}_2$ behaviour.

they should, the two evidently agree very well (though the $\mathcal{O}(\ln L/L)$ finite-size corrections of Eq. 63 for $\xi \ll 1$ are just about discernible). The figure also shows clearly both the large- ξ behaviour $\tau_q \propto 1/\xi$ (Eqs. 61,64), and the small- ξ limiting behaviour $\tau_q = (q-1)/(2\ln 2)$ (Eq. 63). The left panel of Fig. 12 shows the corresponding q-dependence of τ_q obtained from Eqs. 64,65 for a wide range of ξ , from which the non-monotonicity in q that is symptomatic of multifractality is evident. Only for the smallest $\xi = 0.1$ is the behaviour $\tau_q = (q-1)/(2\ln 2)$ seen over the entire q-range shown in practice.

B. Numerical results: hypercube graph

The results above are well supported by ED calculations, obtained in the same way as for the tree graph (Sec. IID), and with the normal distribution for $P_{\mathcal{E}_r}(\mathcal{E}_r)$ as specified after Eq. 52 above.

We have not yet commented on the distribution $P_{\mathcal{L}_q}(\mathcal{L}_q)$ for the hypercube graph. For q=2, Fig. 13 shows $L\times P_{\mathcal{L}_2}(\mathcal{L}_2)$ vs \mathcal{L}_2 obtained from ED (as in Fig. 5 for the tree). Just as for the tree case the distribution is heavy tailed, and the same power-law decay $P_{\mathcal{L}_2}(\mathcal{L}_2) \propto 1/\mathcal{L}_2$ is clearly seen (with the same implications discussed at the end of Sec. II C). One can also deduce this form analytically, in direct parallel to the calculation for the tree in Eq. 35 ff for the case $\xi\gg 1$, where (Eq. 57) $\mathcal{L}_q(r_E)\equiv c_1e^{-c_2r_E}$ has the same form as in Eq. 35. For $\xi\ll 1$, $\mathcal{L}_q(r_E)$ has a different form (Eq. 56); but here too it can be shown that $P_{\mathcal{L}_2}(\mathcal{L}_2)\propto 1/\mathcal{L}_2$.

ED results for $\mathcal{L}_2^{\text{mean}}$ vs L and $\mathcal{L}_2^{\text{typ}}$ vs N are shown in Fig. 14, for a range of disorder strengths W as indicated. These confirm that $\mathcal{L}_2^{\text{mean}} \propto 1/L$, and that $\mathcal{L}_2^{\text{typ}} \propto N^{-\tau_2}$ with a fractal exponent τ_2 which increases with increasing W; and can be compared to their analytical counterparts shown in Fig. 11.

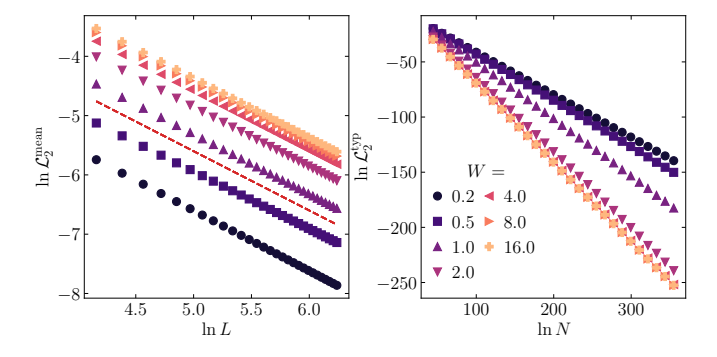


FIG. 14. For the hypercube graph, $\ln \mathcal{L}_2^{\text{mean}}$ (left) and $\ln \mathcal{L}_2^{\text{typ}}$ (right), obtained from ED for different disorder strengths W as indicated. $\ln \mathcal{L}_2^{\text{mean}}$ is plotted against $\ln L$, whereas $\ln \mathcal{L}_2^{\text{typ}}$ is plotted against $\ln N = L \ln 2$. Red dashed line in the left panel for $\ln \mathcal{L}_2^{\text{mean}}$ indicates a slope of -1.

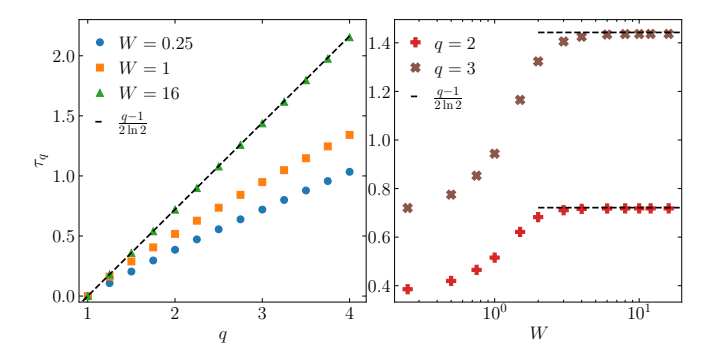


FIG. 15. ED results for multifractal exponents τ_q of the hypercube graph. Left panel: τ_q vs q for W=0.25,1,16. For strong disorder, W=16, the dashed line shows the asymptotic behaviour $(q-1)/(2\ln 2)$. Corresponding analytic results for different ξ are given in Fig. 12 (left panel). Right panel: τ_q vs W, shown for q=2 and q=3. Dashed lines show the asymptote $(q-1)/(2\ln 2)$ (Eq. 63). Analytic results for τ_q vs ξ with q=2,4 are given in Fig. 12 right panel.

Multifractal exponents τ_q obtained from ED are shown in Fig. 15. As in Fig. 14 for q=2, plots of $\ln \mathcal{L}_q^{\mathrm{typ}}$ $vs \ln N$ show clear linearity for any q, enabling $\tau_q=$ $-\ln \mathcal{L}_q^{\text{typ}}/\ln N$ to be read off. For q=2 and 3, the right panel of Fig. 15 shows the evolution of τ_q as a function of W; analytical results for the ξ -dependence of τ_q are shown in Fig. 12 (right panel). For small values of ξ , Eq. 63 predicts the asymptotic behaviour $\tau_q = (q-1)/[2\ln 2]$. That behaviour is indeed seen in the full ED results for strong disorder (reflecting the fact that $\tau_q = (q-1)/[2 \ln 2]$ does not per se depend on ξ , so should hold for sufficiently large disorder strengths W for which $\xi \ll 1$). ED results for τ_q vs q are shown in the left panel of Fig. 15, for W = 0.25, 1, 16; corresponding analytical results for different ξ 's are shown in Fig. 12 (left panel). For strong disorder, W = 16, ED results indeed show the asymptotic behaviour $\tau_q = (q-1)/(2\ln 2)$ over the wide q-range shown, just as they do for the $\xi = 0.1$ case in the left panel of Fig. 12.

V. CONCLUDING REMARKS

We close with a brief summary, and a few remarks by way of outlook. The central outcome of this work is a concrete demonstration – through a combination of analytical and numerical results – of the emergence of robust multifractality in eigenstates of high-dimensional graphs with correlated disorder. Focusing on rooted trees and hypercubes, we introduced a class of disorder correlations, termed radial disorder, in which the site energies are identical for all sites at a given distance from the root, but vary independently across different distances. This correlation pattern was shown to lead to an emergent fragmentation of the graph into one-dimensional chains with uncorrelated disorder. The chain emanating from the root can be naturally identified as the Krylov chain generated from the root-localised initial state.

This structure makes the mechanism underlying the multifractality analytically transparent. The interplay between conventional Anderson localisation along the one-dimensional chain, and the exponential growth in the number of sites with distance from the root (whose linear combinations form the effective chain sites), leads to the multifractality. Since both ingredients are inherently robust, so too is the multifractality. A particularly notable feature is the exceptionally broad distribution of IPRs, which leads to a marked difference between the scalings of the mean and typical IPRs. We find that the mean and typical IPRs scale as power laws with the number of generations and the total number of sites, respectively; implying that it is the latter which defines a multifractal exponent. In short, radial disorder transforms high-dimensional graphs into a natural stage for multifractality to emerge, persist, and be understood.

That being said, it is important to mention that the current work itself introduces the idea and a model of radial disorder in high-dimensional graphs. The results suggest it is likely to provide fertile ground for investigating further aspects of localisation physics thereon, such as the effects on dynamics and transport due to radial disorder. On a more fundamental level, however, it would be of interest to identify and classify the broader class of high-dimensional graphs that can host this phenomenon, and to uncover the deeper mathematical reasons behind it. In the shorter term, it will be instructive to study the impact of perturbatively small additional disorder along the rows of the graph, on top of the radial disorder, by mapping the problem to weakly coupled one-dimensional chains.

ACKNOWLEDGMENTS

DEL expresses his thanks for the hospitality of both the International Centre for Theoretical Sciences (ICTS-TIFR), and the Physics Department, Indian Institute of Science (IISc), Bengaluru. SR acknowledges support from SERB-DST, Government of India, under Grant No. SRG/2023/000858; from the Department of Atomic Energy under Project No. RTI4001; and by a Max Planck

Partner Group grant between ICTS-TIFR, Bengaluru and MPIPKS, Dresden.

- P. W. Anderson, Absence of diffusion in certain random lattices, Phys. Rev. 109, 1492 (1958).
- [2] R. Abou-Chacra, P. W. Anderson, and D. J. Thouless, A self-consistent theory of localization, J. Phys. C 6, 1734 (1973).
- [3] E. Abrahams, P. W. Anderson, D. C. Licciardello, and T. V. Ramakrishnan, Scaling theory of localization: Absence of quantum diffusion in two dimensions, Phys. Rev. Lett. 42, 673 (1979).
- [4] P. A. Lee and T. V. Ramakrishnan, Disordered electronic systems, Rev. Mod. Phys. 57, 287 (1985).
- [5] F. Evers and A. D. Mirlin, Anderson transitions, Rev. Mod. Phys. 80, 1355 (2008).
- [6] I. García-Mata, O. Giraud, B. Georgeot, J. Martin, R. Dubertrand, and G. Lemarié, Scaling theory of the Anderson transition in random graphs: Ergodicity and universality, Phys. Rev. Lett. 118, 166801 (2017).
- [7] I. García-Mata, J. Martin, R. Dubertrand, O. Giraud, B. Georgeot, and G. Lemarié, Two critical localization lengths in the Anderson transition on random graphs, Phys. Rev. Research 2, 012020 (2020).
- [8] I. García-Mata, J. Martin, O. Giraud, B. Georgeot, R. Dubertrand, and G. Lemarié, Critical properties of the Anderson transition on random graphs: Two-parameter scaling theory, Kosterlitz-Thouless type flow, and manybody localization, Phys. Rev. B 106, 214202 (2022).
- [9] C. Vanoni, B. L. Altshuler, V. E. Kravtsov, and A. Scardicchio, Renormalization group analysis of the Anderson model on random regular graphs, Proceedings of the National Academy of Sciences 121, e2401955121 (2024).
- [10] B. L. Altshuler, V. E. Kravtsov, A. Scardicchio, P. Sierant, and C. Vanoni, Renormalization group for Anderson localization on high-dimensional lattices (2024), arXiv:2403.01974 [cond-mat.dis-nn].
- [11] D. M. Basko, I. L. Aleiner, and B. L. Altshuler, Metalinsulator transition in a weakly interacting many-electron system with localized single-particle states, Annals of Physics 321, 1126 (2006).
- [12] I. V. Gornyi, A. D. Mirlin, and D. G. Polyakov, Interacting electrons in disordered wires: Anderson localization and low-T transport, Phys. Rev. Lett. 95, 206603 (2005).
- [13] V. Oganesyan and D. A. Huse, Localization of interacting fermions at high temperature, Phys. Rev. B 75, 155111 (2007).
- [14] R. Nandkishore and D. A. Huse, Many-body localization and thermalization in quantum statistical mechanics, Annu. Rev. Condens. Matter Phys. 6, 15 (2015).
- [15] D. A. Abanin and Z. Papić, Recent progress in manybody localization, Annalen der Physik 529, 1700169 (2017).
- [16] D. A. Abanin, E. Altman, I. Bloch, and M. Serbyn, Colloquium: Many-body localization, thermalization, and entanglement, Rev. Mod. Phys. 91, 021001 (2019).
- [17] P. Sierant, M. Lewenstein, A. Scardicchio, L. Vidmar, and J. Zakrzewski, Many-body localization in the age of classical computing, Reports on Progress in Physics 88,

- 026502 (2025).
- [18] D. E. Logan and P. G. Wolynes, Quantum localization and energy flow in many-dimensional Fermi resonant systems, J. Chem. Phys. 93, 4994 (1990).
- [19] B. L. Altshuler, Y. Gefen, A. Kamenev, and L. S. Levitov, Quasiparticle lifetime in a finite system: A nonperturbative approach, Phys. Rev. Lett. 78, 2803 (1997).
- [20] C. Monthus and T. Garel, Many-body localization transition in a lattice model of interacting fermions: Statistics of renormalized hoppings in configuration space, Phys. Rev. B 81, 134202 (2010).
- [21] F. Pietracaprina, V. Ros, and A. Scardicchio, Forward approximation as a mean-field approximation for the Anderson and many-body localization transitions, Phys. Rev. B 93, 054201 (2016).
- [22] G. Biroli and M. Tarzia, Delocalized glassy dynamics and many-body localization, Phys. Rev. B 96, 201114 (2017).
- [23] A. Altland and T. Micklitz, Field Theory Approach to Many-Body Localization, Phys. Rev. Lett. 118, 127202 (2017).
- [24] D. E. Logan and S. Welsh, Many-body localization in Fock space: A local perspective, Phys. Rev. B 99, 045131 (2019).
- [25] S. Roy and D. E. Logan, Fock-space correlations and the origins of many-body localization, Phys. Rev. B 101, 134202 (2020).
- [26] K. S. Tikhonov and A. D. Mirlin, Eigenstate correlations around the many-body localization transition, Phys. Rev. B 103, 064204 (2021).
- [27] G. De Tomasi, I. M. Khaymovich, F. Pollmann, and S. Warzel, Rare thermal bubbles at the many-body localization transition from the Fock space point of view, Phys. Rev. B 104, 024202 (2021).
- [28] S. Roy and D. E. Logan, Fock-space anatomy of eigenstates across the many-body localization transition, Phys. Rev. B 104, 174201 (2021).
- [29] M. Tarzia, Many-body localization transition in Hilbert space, Phys. Rev. B 102, 014208 (2020).
- [30] J. Sutradhar, S. Ghosh, S. Roy, D. E. Logan, S. Mukerjee, and S. Banerjee, Scaling of the Fock-space propagator and multifractality across the many-body localization transition, Phys. Rev. B 106, 054203 (2022).
- [31] S. Roy, Anatomy of localisation protected quantum order on Hilbert space, Journal of Physics: Condensed Matter 35, 415601 (2023).
- [32] N. Roy, J. Sutradhar, and S. Banerjee, Diagnostics of nonergodic extended states and many body localization proximity effect through real-space and Fock-space excitations, Phys. Rev. B 107, 115155 (2023).
- [33] J.-N. Herre, J. F. Karcher, K. S. Tikhonov, and A. D. Mirlin, Ergodicity-to-localization transition on random regular graphs with large connectivity and in many-body quantum dots, Phys. Rev. B 108, 014203 (2023).
- [34] M. Schiró and M. Tarzia, Toy model for anomalous transport and Griffiths effects near the many-body localization transition, Phys. Rev. B 101, 014203 (2020).
- [35] T. Scoquart, I. V. Gornyi, and A. D. Mirlin, Role of Fock-

- space correlations in many-body localization, Phys. Rev. B 109, 214203 (2024).
- [36] S. Ghosh, J. Sutradhar, S. Mukerjee, and S. Banerjee, Scaling of Fock space propagator in quasiperiodic manybody localizing systems (2024), arXiv:2401.03027 [condmat.dis-nn].
- [37] K. Tikhonov and A. Mirlin, From Anderson localization on random regular graphs to many-body localization, Annals of Physics 435, 168525 (2021).
- [38] S. Roy and D. E. Logan, The Fock-space landscape of many-body localisation, Journal of Physics: Condensed Matter 37, 073003 (2024).
- [39] A. De Luca and A. Scardicchio, Ergodicity breaking in a model showing many-body localization, Europhys. Lett. 101, 37003 (2013).
- [40] G. Biroli and M. Tarzia, Delocalized glassy dynamics and many-body localization, Phys. Rev. B 96, 201114 (2017).
- [41] G. Biroli and M. Tarzia, Anomalous dynamics on the ergodic side of the many-body localization transition and the glassy phase of directed polymers in random media, Phys. Rev. B 102, 064211 (2020).
- [42] S. Roy and D. E. Logan, Localization on Certain Graphs with Strongly Correlated Disorder, Phys. Rev. Lett. 125, 250402 (2020).
- [43] G. Biroli, A. K. Hartmann, and M. Tarzia, Largedeviation analysis of rare resonances for the many-body localization transition, Phys. Rev. B 110, 014205 (2024).
- [44] D. J. Luitz, N. Laflorencie, and F. Alet, Many-body localization edge in the random-field Heisenberg chain, Phys. Rev. B 91, 081103 (2015).
- [45] N. Macé, F. Alet, and N. Laflorencie, Multifractal scalings across the many-body localization transition, Phys. Rev. Lett. 123, 180601 (2019).
- [46] N. Rosenzweig and C. E. Porter, Repulsion of energy levels in complex atomic spectra, Phys. Rev. 120, 1698 (1960).
- [47] A. D. Mirlin, Y. V. Fyodorov, F.-M. Dittes, J. Quezada, and T. H. Seligman, Transition from localized to extended eigenstates in the ensemble of power-law random banded matrices, Phys. Rev. E 54, 3221 (1996).
- [48] V. Kravtsov, I. Khaymovich, E. Cuevas, and M. Amini, A random matrix model with localization and ergodic transitions, New J. Phys. 17, 122002 (2015).
- [49] L. F. Cugliandolo, G. Schehr, M. Tarzia, and D. Venturelli, Multifractal phase in the weighted adjacency matrices of random Erdös-Rényi graphs, Phys. Rev. B 110, 174202 (2024).
- [50] J. T. Chalker, Scaling and correlations at a mobility edge in two dimensions, Journal of Physics C: Solid State Physics 21, L119 (1988).
- [51] J. T. Chalker, Scaling and eigenfunction correlations near a mobility edge, Physica A: Statistical Mechanics and its Applications 167, 253 (1990).
- [52] A. W. W. Ludwig, M. P. A. Fisher, R. Shankar, and G. Grinstein, Integer quantum Hall transition: An alternative approach and exact results, Phys. Rev. B 50, 7526 (1994).
- [53] B. Huckestein, Scaling theory of the integer quantum Hall effect, Rev. Mod. Phys. 67, 357 (1995).
- [54] F. Evers, A. Mildenberger, and A. D. Mirlin, Multifractality of wave functions at the quantum Hall transition revisited, Phys. Rev. B 64, 241303 (2001).
- [55] A. D. Mirlin and F. Evers, Multifractality and critical fluctuations at the Anderson transition, Phys. Rev. B

- **62**, 7920 (2000).
- [56] K. S. Tikhonov and A. D. Mirlin, Critical behavior at the localization transition on random regular graphs, Phys. Rev. B 99, 214202 (2019).
- [57] P. A. Nosov, I. M. Khaymovich, and V. E. Kravtsov, Correlation-induced localization, Phys. Rev. B 99, 104203 (2019).
- [58] A. Duthie, S. Roy, and D. E. Logan, Anomalous multifractality in quantum chains with strongly correlated disorder, Phys. Rev. B 106, L020201 (2022).
- [59] M. R. Zirnbauer, Localization transition on the Bethe lattice, Phys. Rev. B 34, 6394 (1986).
- [60] J. T. Chalker and S. Siak, Anderson localisation on a Cayley tree: a new model with a simple solution, J. Phys.: Cond. Matt. 2, 2671 (1990).
- [61] A. D. Mirlin and Y. V. Fyodorov, Localization transition in the Anderson model on the Bethe lattice: Spontaneous symmetry breaking and correlation functions, Nuclear Physics B 366, 507 (1991).
- [62] B. Derrida and G. J. Rodgers, Anderson model on a Cayley tree: the density of states, Journal of Physics A: Mathematical and General 26, L457 (1993).
- [63] C. Monthus and T. Garel, Anderson transition on the Cayley tree as a traveling wave critical point for various probability distributions, Journal of Physics A: Mathematical and Theoretical 42, 075002 (2008).
- [64] C. Monthus and T. Garel, Anderson localization on the Cayley tree: multifractal statistics of the transmission at criticality and off criticality, J. Phys. A 44, 145001 (2011).
- [65] K. S. Tikhonov and A. D. Mirlin, Fractality of wave functions on a Cayley tree: Difference between tree and locally treelike graph without boundary, Phys. Rev. B 94, 184203 (2016).
- [66] V. Kravtsov, B. Altshuler, and L. Ioffe, Non-ergodic delocalized phase in Anderson model on Bethe lattice and regular graph, Annals of Physics 389, 148 (2018).
- [67] S. Savitz, C. Peng, and G. Refael, Anderson localization on the Bethe lattice using cages and the Wegner flow, Phys. Rev. B 100, 094201 (2019).
- [68] G. Parisi, S. Pascazio, F. Pietracaprina, V. Ros, and A. Scardicchio, Anderson transition on the Bethe lattice: an approach with real energies, Journal of Physics A: Mathematical and Theoretical 53, 014003 (2019).
- [69] B. Derrida, Random-energy model: Limit of a family of disordered models, Phys. Rev. Lett. 45, 79 (1980).
- [70] C. R. Laumann, A. Pal, and A. Scardicchio, Many-body mobility edge in a mean-field quantum spin glass, Phys. Rev. Lett. 113, 200405 (2014).
- [71] C. L. Baldwin, C. R. Laumann, A. Pal, and A. Scardicchio, The many-body localized phase of the quantum random energy model, Phys. Rev. B 93, 024202 (2016).
- [72] S. Aubry and G. André, Analyticity breaking and Anderson localization in incommensurate lattices, Ann. Israel Phys. Soc 3, 18 (1980).
- [73] V. Balasubramanian, P. Caputa, J. M. Magan, and Q. Wu, Quantum chaos and the complexity of spread of states, Phys. Rev. D 106, 046007 (2022).
- [74] V. Balasubramanian, J. M. Magan, and Q. Wu, Tridiagonalizing random matrices, Phys. Rev. D 107, 126001 (2023)
- [75] M. Gautam, K. Pal, K. Pal, A. Gill, N. Jaiswal, and T. Sarkar, Spread complexity evolution in quenched interacting quantum systems, Phys. Rev. B 109, 014312

- (2024).
- [76] P. Nandy, A. S. Matsoukas-Roubeas, P. Martínez-Azcona, A. Dymarsky, and A. del Campo, Quantum dynamics in Krylov space: Methods and applications, Physics Reports 1125-1128, 1 (2025).
- [77] P. G. Harper, Single band motion of conduction electrons in a uniform magnetic field, Proceedings of the Physical Society. Section A 68, 874 (1955).
- [78] D. J. Thouless, Bandwidths for a quasiperiodic tightbinding model, Phys. Rev. B 28, 4272 (1983).
- [79] R. E. Prange, D. R. Grempel, and S. Fishman, Wave functions at a mobility edge: An example of a singular continuous spectrum, Phys. Rev. B 28, 7370 (1983).
- [80] S. Das Sarma, S. He, and X. C. Xie, Mobility edge in a model one-dimensional potential, Phys. Rev. Lett. 61, 2144 (1988).
- [81] D. J. Boers, B. Goedeke, D. Hinrichs, and M. Holthaus, Mobility edges in bichromatic optical lattices, Phys. Rev. A 75, 063404 (2007).
- [82] J. Biddle, B. Wang, D. J. Priour, and S. Das Sarma, Localization in one-dimensional incommensurate lattices beyond the Aubry-André model, Phys. Rev. A 80, 021603 (2009).
- [83] S. Ganeshan, J. H. Pixley, and S. Das Sarma, Nearest neighbor tight binding models with an exact mobility edge in one dimension, Phys. Rev. Lett. 114, 146601 (2015).
- [84] H. Yao, A. Khoudli, L. Bresque, and L. Sanchez-Palencia, Critical behavior and fractality in shallow onedimensional quasiperiodic potentials, Phys. Rev. Lett. 123, 070405 (2019).
- [85] Y. Wang, X. Xia, L. Zhang, H. Yao, S. Chen, J. You, Q. Zhou, and X.-J. Liu, One-dimensional quasiperiodic mosaic lattice with exact mobility edges, Phys. Rev. Lett. 125, 196604 (2020).
- [86] A. Duthie, S. Roy, and D. E. Logan, Self-consistent theory of mobility edges in quasiperiodic chains, Phys. Rev. B 103, L060201 (2021).
- [87] E. N. Economou, Green's Functions in Quantum Physics (Springer, Berlin, 2006).